

# Analysis of turbulence characteristics in a temporal dense gas compressible mixing layer using direct numerical simulation

Aurélien Vadrot<sup>1,†</sup>, Alexis Giauque<sup>1</sup> and Christophe Corre<sup>1</sup>

<sup>1</sup>LMFA – Laboratoire de Mécanique des Fluides et d’Acoustique, Ecole Centrale de Lyon, 36 avenue Guy de Collongue, 69134 Ecully CEDEX, France

(Received 1 August 2019; revised 21 December 2019; accepted 15 March 2020)

This study investigates the effects of a Bethe–Zel’dovich–Thompson (BZT) dense gas (FC-70) on the development of a turbulent compressible mixing layer at a convective Mach number  $M_c = 1.1$ . Three-dimensional direct numerical simulations are performed with both FC-70 and air. The initial thermodynamic state for FC-70 lies inside the inversion region where the fundamental derivative of gas dynamics ( $\Gamma$ ) becomes negative. The complex Martin–Hou thermodynamic equation of state is used to reproduce thermodynamic peculiarities of the BZT dense gas (DG). The unstable growth phase in the mixing layer development shows an increase of  $xy$ -turbulent stress tensors in DG compared to perfect gas (PG). The following self-similar period has been carefully defined from the time evolution of the integrated streamwise production and transport terms. During the self-similar stage, DG and PG mixing layers at  $M_c = 1.1$  display close values of the momentum thickness growth rate, which seems similarly affected by the well-known compressibility-related reduction for PG. The same mechanisms are at stake, related to the reduction of pressure–strain terms. Turbulent kinetic energy (TKE) spectra show a slower decrease of TKE at small scales for DG compared with PG. The filtered kinetic energy equation balance developed by Aluie (*Physica D*, vol. 247 (1), 2013, pp. 54–65) is applied for the first time to a compressible mixing layer. The equation is reshaped to better account for TKE transport across the mixing layer. This new formulation brings out the role played by  $\Sigma_l$ , the pressure strengths power. A detailed comparison of the contributions to the filtered TKE equation is provided for both PG and DG mixing layers.

**Key words:** compressible turbulence, shear layer turbulence, turbulence simulation

---

## 1. Introduction

Dense gases (DGs) have been widely studied during the past forty years because of their increasing use as working fluids in organic Rankine cycles (ORCs), which collect heat from low-temperature heat sources (solar, geothermal, biomass combustion, etc.) in order to produce electricity. Using DGs in ORC power plants has many benefits

<sup>†</sup> Email address for correspondence: [aurelien.vadrot@ec-lyon.fr](mailto:aurelien.vadrot@ec-lyon.fr)

(lower operating pressure, reduction of blade corrosion, large heat capacities, etc.), the main one being the lower boiling temperature compared with water, which enables operation with targeted lower-temperature heat sources. For comparable reasons, DGs are also used in Stirling engines (Invernizzi 2010), hypersonic and supersonic wind tunnels (Wagner & Schmidt 1978; Anders, Anderson & Murthy 1999) and chemical transport and processing (Kirillov 2004).

Dense gases are single-phase vapours characterized by long chains of carbon atoms and by a medium to large molar mass. In the vicinity of the critical point, DGs exhibit an unusual behaviour compared with classical gases. In this study, specific DGs called Bethe–Zel’dovich–Thompson (BZT) gases are considered. The name BZT was given by Cramer (1991) to acknowledge the pioneering works of Bethe (1942), Zel’dovich (1946) and Thompson (1971) on these gases which are also widely used in industry. Examples of BZT gases include hydrocarbons, perfluorocarbons and siloxanes. The BZT gases display an ‘inversion zone’, that is, a thermodynamic region where the fundamental derivative of gas dynamics becomes negative ( $\Gamma < 0$ ).

The fundamental derivative of gas dynamics was introduced by Hayes (1958), and then rewritten by Thompson (1971) as

$$\Gamma = \frac{v^3}{2c^2} \frac{\partial^2 p}{\partial v^2} \Big|_s = \frac{c^4}{2v^3} \frac{\partial^2 v}{\partial p^2} \Big|_s = 1 + \frac{\rho}{c} \frac{\partial c}{\partial \rho} \Big|_s, \quad (1.1)$$

where  $v$  is the specific volume,  $\rho$  the density,  $c = \sqrt{\partial p / \partial \rho}|_s$  the speed of sound,  $p$  the pressure and  $s$  the entropy. The term ‘fundamental’ emphasizes the importance of  $\Gamma$  in the determination of the nonlinear behaviour of DGs. This physical quantity is a measure of the rate of change of the speed of sound in an isentropic transformation. It is directly related to the curvature of isentropic curves in the  $p$ – $v$  diagram ( $\partial^2 p / \partial v^2|_s$ ).

There are three main regimes depending on the value of the fundamental derivative:

- (i) Regime  $\Gamma > 1$  corresponds to classical ideal gas behaviour. For thermally and calorically perfect gases, the fundamental derivative is a constant and given by  $\Gamma = (\gamma + 1)/2$ .
- (ii) Regime  $0 < \Gamma < 1$  corresponds to classical non-ideal gas behaviour. In this regime, the speed of sound decreases in isentropic compressions ( $\partial c / \partial \rho|_s < 0$ ).
- (iii) Regime  $\Gamma < 0$  corresponds to non-classical behaviour referred to as the BZT effect. It is a narrow region in the  $p$ – $v$  diagram as shown in figure 1. In that zone, because of the negative sign of the fundamental derivative, rarefaction shock waves can occur.

Bethe (1942) and Zel’dovich (1946) were the first to justify this possible occurrence of expansion shock waves in BZT flows. Such unusual features can only be modelled when using a sufficiently complex equation of state (EoS). The simplest EoS enabling the prediction of expansion shock waves is the van der Waals EoS. In the vicinity of the critical point, the isothermal curves (for example the critical one) display a negative curvature (concave), so that  $\partial^2 p / \partial v^2|_T < 0$ . Using one of Maxwell’s relations:

$$\frac{\partial T}{\partial v} \Big|_s = - \frac{\partial p}{\partial s} \Big|_v = - \frac{\partial p}{\partial T} \Big|_v \frac{\partial T}{\partial s} \Big|_v = - \frac{\frac{\partial p}{\partial T} \Big|_v}{\frac{\partial s}{\partial T} \Big|_v} = - \frac{T}{c_v} \left( \frac{\partial p}{\partial T} \right)_v \quad (1.2)$$

justifies that if the heat capacity is large ( $c_v \gg 1$ ), the isentropic curves will follow the isothermal ones ( $\partial T / \partial v|_s \ll 1$ ). Colonna & Guardone (2006) provided further

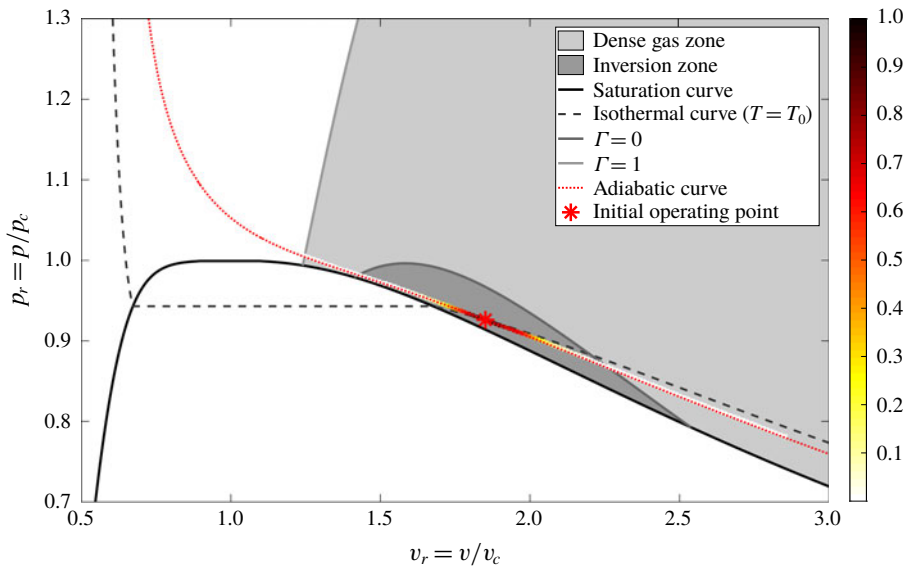


FIGURE 1. The initial thermodynamic state and its evolution over time are represented in the non-dimensional  $p$ - $v$  diagram for FC-70. The DG zone ( $\Gamma < 1$ ) and the inversion zone ( $\Gamma < 0$ ) are plotted for the Martin–Hou equation of state. Parameters  $p_c$  and  $v_c$  are, respectively, the critical pressure and the critical specific volume. The initial value of the fundamental derivative of gas dynamics is  $\Gamma_{initial} = -0.284$ . The normalized distribution of thermodynamic states at  $\tau = 1700$  (beginning of the self-similar period) is coloured along the corresponding adiabatic curve.

explanations using an advanced molecular study of forces at stake, depending on the molecular complexity. They showed that the minimum molecular complexity that must be reached in a gas in order to fulfil the BZT gas conditions is  $N > N^{BZT} = 33.33$ , with  $N$  being the molecular complexity corresponding to the number of active degrees of freedom of the molecule (Colonna & Guardone 2006).

Many researchers have studied the non-classical phenomena occurring in (BZT) DGs, such as rarefaction shock waves, by considering at first the fluid as inviscid (Cramer & Kluwick 1984; Menikoff & Plohr 1989; Rusak & Wang 1997; Wang & Rusak 1999; Congedo, Corre & Cinnella 2007, 2011). Adding viscosity effects enabled the study of boundary layers and shock–boundary layer interactions (Cramer & Crickenberger 1991; Cramer & Park 1999; Ferguson & Argrow 2001; Kluwick 2004). Conclusions show the benefits of using DGs in ORC turbines since, when operating in the dense gas region ( $0 < \Gamma < 1$ ) at transonic regime, DG effects reduce friction drag and boundary layer separation (Cinnella & Congedo 2007). Also, when the expansion operates within the inversion region ( $\Gamma < 0$ ), shock intensity decreases and entropy losses are reduced.

From an experimental viewpoint, it is very difficult to observe rarefaction shock waves because of the vicinity of the critical point where physical quantities experience strong variations. Borisov *et al.* (1983) and Kutateladze, Nakoryakov & Borisov (1987) claimed to have experimentally observed rarefaction shock waves. However, their results were questioned by Cramer & Sen (1986) and Ferguson *et al.* (2001) who showed that the fluid used in the experiment (F-13,  $\text{CCIF}_3$ ) does not satisfy the

Thompson & Lambrakis (1973) requirements and concluded that the observed shock wave was not a single-phase rarefaction shock wave.

Since then, works of Ferguson *et al.* (2001), Colonna *et al.* (2008), Spinelli *et al.* (2010) and Spinelli *et al.* (2013) enabled the design of shock tubes and test rigs, such as the Test Rig for Organic Vapors (TROVA) at Politecnico di Milano or the Flexible Asymmetric Shock Tube (FAST) built at Delft University of Technology (Mathijssen *et al.* 2015). The experimental proof of rarefaction shock waves remains an active research area.

From a numerical viewpoint, Argrow (1996) was the first to perform a numerical simulation of a single-phase DG inviscid flow in a shock tube. This pioneering work on the simulation of inviscid DG flows was followed by contributions of Monaco, Cramer & Watson (1997), Brown & Argrow (1998), Colonna & Rebay (2004) and Cinnella & Congedo (2005) with the simulation of inviscid DG flows over airfoils or turbine cascades. Cinnella & Congedo (2007) performed for the first time DG simulations for laminar and turbulent external flows over airfoils and flat plates using Reynolds-averaged Navier–Stokes equations with the simple algebraic model of Baldwin and Lomax in the latter case. Harinck *et al.* (2010*b*), Wheeler & Ong (2013) and From *et al.* (2017) subsequently achieved simulations of turbulent DG flows using, respectively,  $k$ – $\varepsilon$  and  $k$ – $\omega$  two-equation models, Spalart–Allamaras one-equation model and an explicit algebraic Reynolds stress model. Dura Galiana, Wheeler & Ong (2016) also performed large-eddy simulations (LES) of turbulent DG flow over a turbine vane using the Smagorinsky–Lilly model. Up to now, the closure of the Reynolds-averaged Navier–Stokes equations or the filtered Navier–Stokes equations originally established for ideal gas flows has been implicitly extended to turbulent DG flows. It can be argued that the peculiar thermodynamic behaviour of DGs, in particular BZT gases, questions the validity of this extension. Yet, the lack of experimental data makes the verification of the presently used turbulence models a complex task. Note that the influence of the thermodynamic models on the numerical prediction of DG flows is also an issue that has been investigated by several authors (e.g. Harinck *et al.* 2010*a*; Merle & Cinnella 2014) and suffers from the same lack of reference experimental data. In the present study, the Martin–Hou (MH) EoS will be retained since it has been established that it provides an accurate representation of DG thermodynamic behaviour (Guardone, Vigevano & Argrow 2004).

The tool of choice to be used in order to assess the potential specificities of turbulence in a DG flow is direct numerical simulation (DNS), which enables the resolution of every turbulent scale, from the largest swirls (limited by the size of the domain) to the smallest ones (limited by the Kolmogorov scale), and thus gives access to the flow physics without resorting to any turbulent closure model. Because the number of degrees of turbulence grows faster than  $O(Re^{11/4})$  (Garnier, Adams & Sagaut 2009), DNS remains naturally confined to simple flow configurations. For larger and more complex systems, LES is a tool of choice since it resolves large turbulent scales and models the small ones. However, as already mentioned, it relies on subgrid models which have been tailored for turbulent flows of ideal gases so that their validity for DGs is also questionable.

At the present time, few authors have achieved DNS of DG flows. Giauque, Corre & Menghetti (2017) have performed a DNS of decaying homogeneous isotropic turbulence (HIT) and concluded that the standard Smagorinski subgrid-scale (SGS) model does not capture correctly the temporal evolution of the turbulent kinetic energy (TKE) by comparing the LES prediction with the DNS reference results. The DNS also evidenced localized flow regions with strongly positive values for the velocity divergence that could correspond to expansion shock waves.

Sciacovelli *et al.* (2016) have also studied the large-scale dynamics in decaying HIT, assuming at first an inviscid DG. They evidenced strong differences of the fluctuation levels for thermodynamic quantities (density, pressure, sound speed) between the perfect gas (PG) and the DG. They pointed out the more symmetric probability density function of the velocity divergence in the DG flow. Their DNS results display flow regions with strong expansions and tubular structures unlike the compression regions which are characterized by sheet-like structures. The more symmetric distribution could be explained by the presence of expansion shock waves.

Sciacovelli, Cinnella & Grasso (2017*b*) next extended their previous decaying HIT study by considering viscous effects and focused then on the small-scale dynamics. Two different initial states were selected for the DG: one inside the inversion region and one outside. It was observed that the global flow dynamics is almost not influenced by local events such as expansion shock waves. The nature of turbulent structures was also discussed based on DNS results. The formation of convergent compressed structures like compression shock waves is strongly reduced in the BZT zone. The occurrence of non-focal convergent structures in the DG diminishes the vorticity and counterbalances enstrophy destruction.

Sciacovelli, Cinnella & Gloerfelt (2017*a*) achieved the DNS of a supersonic DG flow in a channel. Significant differences from a supersonic ideal gas channel flow were observed for some thermodynamic variables. For instance, the temperature is lower at the centreline for the DG and the DG flow can actually be considered quasi-isothermal contrary to the PG flow. Characteristics of the DG flow have been found to be close to those of flow of variable-property liquids. Regarding turbulence development, the authors did not notice significant differences between the PG and the DG. The Reynolds stresses and the non-dimensional streamwise and spanwise lengths of the structures are found to be nearly the same.

So far, no DNS of a DG compressible mixing layer has been reported in the literature. Performing such a DNS enables a better understanding of DG behaviour in a simple configuration which is also representative of a flow configuration occurring inside an ORC turbine. While the decaying HIT can be seen as representative of a small flow region in the inter-blade space, the mixing layer would be representative of the blade wake region. Also, the speed of sound in a DG being likely to be much lower (up to 10 times lower) than in a usual gas such as air, the Mach number characterizing the DG compressible mixing layer can become large. A review of the literature has been performed in order to select a reference ideal gas compressible mixing layer at a large Mach number and also to identify some key results regarding the compressible mixing layer of an ideal gas, with which the DG DNS results will be confronted.

Mixing layer studies belong to a long-term research programme on the characterization of turbulence. Turbulent mixing layers appear in many physical domains and industry problems. The very first investigation of turbulent mixing layers was performed by Liepmann & Laufer (1947) who demonstrated the self-preserving feature of such flows. Subsequently, many experimental investigations were conducted on turbulent mixing layers, especially for aeronautic purposes, such as scram-jet engines and abatement of supersonic jet noise.

Quickly, compressibility effects proved to be a key point in high-speed mixing layer flows. Bogdanoff (1983) introduced the concept of the convective Mach number, taking into account not only the velocity and sound speed of each stream of the mixing layer but also a combination of them. Denoting  $U_i$  and  $c_i$ , respectively, as the

flow speed and the sound speed of stream  $i$  (upper or lower) of the mixing layer, the convective Mach number is defined as

$$M_c = (U_1 - U_2)/(c_1 + c_2) = \Delta u/(c_1 + c_2). \quad (1.3)$$

The convective Mach number provided the community with a similar comparative scale when comparing different configurations. A consensus appeared on the reduction of the mixing layer growth rate when increasing the convective Mach number (Bradshaw 1977; Papamoschou & Roshko 1988).

Further studies were conducted in order to capture the key parameters allowing a better understanding of the fundamental mechanisms at stake. Brown & Roshko (1974) investigated density effects using two different gases and thoroughly analysed turbulent structures to conclude that density effects are far less prominent than compressibility effects. Although the mixing layer flow configuration appears rather simple, Bradshaw (1966) showed that initial conditions and technical difficulties with the experimental realization of the flow are the main sources of the discrepancies observed between published results.

The first DNS of a compressible mixing layer was performed by Sandham & Reynolds (1990), followed by Luo & Sandham (1994), Vreman, Sandham & Luo (1996), Freund, Lele & Moin (2000), Pantano & Sarkar (2002), Fu & Li (2006), Zhou, He & Shen (2012), Martínez Ferrer, Lehnasch & Mura (2017) and Dai *et al.* (2018). These DNS of compressible mixing layers assume the fluid behaves like an ideal gas. They all confirm that the spreading rate decay is due to a lower turbulent production (Sarkar 1995). The compressible TKE equation includes additional terms with respect to its incompressible formulation, namely compressible dissipation and pressure–dilatation terms. Key questions, seemingly related, are why turbulent production decreases and how these additional terms evolve with an increasing convective Mach number.

Zeman (1990) and Sarkar *et al.* (1991) predicted that the dilatational part of the dissipation increases with the turbulent Mach number ( $M_t = \sqrt{u_i' u_i'}/c$ , where  $u_i'$  represents the fluctuating velocity in direction  $i$ ) because of the occurrence of eddy shocklets. They proposed a modelling of this term that captures the growth rate reduction as the Mach number increases. However, Vreman *et al.* (1996) and Freund *et al.* (2000) suggested that the proposed model is not realistic since eddy shocklets at that time had not yet been observed in three-dimensional DNS with a convective Mach number below one. Subsequently, Zhou *et al.* (2012) observed shocklets in their three-dimensional simulation for a convective Mach number of 0.7. Although eddy shocklets may occur in the compressible mixing layer for a convective Mach number as low as 0.7, the compressible dissipation term remains small as shown by Pantano & Sarkar (2002) for a convective Mach number of 1.1 and below. We will see that this observation is confirmed by the present simulations. Considering a DG instead of an ideal gas should even further reduce this dissipation term since entropy jumps across shocklets are reduced within the inversion region.

The pressure–dilatation term is formed from the sum of the pressure–strain rate correlations. It is negligible if compared with the most important terms of the TKE equation (Vreman *et al.* 1996; Freund *et al.* 2000; Pantano & Sarkar 2002). However, each pressure–strain correlation is far from being negligible and the decrease of these correlations with an increasing Mach number is likely to explain the decay of the growth rate (Vreman *et al.* 1996; Freund *et al.* 2000). Vreman *et al.* (1996) proposed a model of the pressure–strain rate correlations and Freund *et al.* (2000) explained



	$T_c$ (K)	$p_c$ (atm)	$Z_c$	$T_b$ (K)	$m (=c_v(T_c)/R)$	$n$
FC-70	608.2	10.2	0.270	488.2	118.7	0.493

TABLE 1. Physical parameters of FC-70 (Cramer 1989). The critical pressure  $p_c$ , the critical temperature  $T_c$ , the boiling temperature  $T_b$  and the compressibility factor  $Z_c = p_c v_c / (RT_c)$  are the input data for the MH equation. The critical specific volume  $v_c$  is deduced from the aforementioned parameters. The acentric factor  $n$  and the  $c_v(T_c)/R$  ratio are used to compute the heat capacity  $c_v(T)$  ( $R = \mathcal{R}/M$  being the specific gas constant computed from the universal gas constant  $\mathcal{R}$  with  $M$  being the molar mass of the gas).

the decay of turbulent quantities by an abatement of pressure fluctuations causing a communication breakdown across the large structures. Further explanations are given by the sonic-eddy model of Breidenthal (1992). Since pressure–strain correlations are composed of pressure fluctuations and strain-rate fluctuations, Martínez Ferrer *et al.* (2017) suggested that the reduction of pressure fluctuations may not be the only reason for the pressure–strain rate decay. Their three-dimensional DNS simulations at convective Mach numbers between 0.35 and 1.1 suggest that the strain-rate fluctuations also decrease with an increasing Mach number.

In the present article, the influence of a DG on the turbulent quantities characteristic of the mixing layer and in particular on the mixing layer growth rate is investigated for the first time using DNS for a convective Mach number of 1.1. This rather large value is retained because it can be expected for DG mixing layers in practical applications and also because several ideal gas DNS are available for this value of  $M_c$ , which will allow the validation of our own ideal gas DNS.

The next section describes the main parameters of the numerical study. The present DNS results are then validated in § 3 for an air compressible mixing layer at  $M_c = 1.1$ . Finally, comparisons between ideal gas and DG mixing layers are performed in § 4. The analysis focuses on the TKE balance, the specific TKE spectra and the filtered kinetic energy balance. The aim is to analyse the differences, if any, in the integrated turbulent terms but also over the whole spectrum, by looking at the key turbulent quantities over the turbulent scales.

## 2. Problem description

### 2.1. Initial conditions

Direct numerical simulations of an  $M_c = 1.1$  compressible mixing layer are performed for a PG and for a (BZT) DG. In the first case, air is chosen and considered as a PG as done by Freund *et al.* (2000). For the DG simulations, perfluorotripropylamine (FC-70,  $C_{15}F_{33}N$ ) is used. It is the same DG used by Ferguson *et al.* (2001) in order to simulate rarefaction shock waves in a shock tube. It is in particular used as heat transfer fluid, is almost non-toxic and has been evaluated as synthetic blood (Costello, Flynn & Owens 2000). Physical parameters useful for the thermodynamic description of FC-70 are given in table 1, as taken from Cramer (1989).

The initial conditions of the mixing layer require the choice of the initial operating thermodynamic point in the  $p$ – $v$  diagram. As described in figure 1, this initial state is chosen within the inversion zone of FC-70 in order to favour the occurrence of expansion shocklets and to maximize DG effects on turbulence. This is also in that region that compressibility effects are the largest since the sound speed is reduced (Colonna & Guardone 2006), which maximizes the Mach number. Figure 1 also shows

	$M_c$	$\rho_1/\rho_2$	$Re_{\delta_{\theta,0}}$	$L_x \times L_y \times L_z$	$N_x \times N_y \times N_z$	$\Delta u$ (m s <sup>-1</sup> )	$\delta_{\theta,0}$ (nm)
Air	1.1	1.0	160	344 × 172 × 86	512 × 256 × 128 <sup>a</sup>	375.18	12.348
Air	1.1	1.0	160	344 × 172 × 86	1024 × 512 × 256 <sup>b</sup>	375.18	12.348
FC-70	1.1	1.0	160	344 × 172 × 86	512 × 256 × 128 <sup>a</sup>	62.3183	188.18
FC-70	1.1	1.0	160	344 × 172 × 86	1024 × 512 × 256 <sup>b</sup>	62.3183	188.18

TABLE 2. Simulation parameters. Lengths  $L_x$ ,  $L_y$  and  $L_z$  denote computational domain lengths measured in terms of initial momentum thickness and  $N_x$ ,  $N_y$  and  $N_z$  denote the number of grid points. All grids are uniform.

<sup>a</sup>Referred to as the 16.8M simulation, where 16.8M corresponds to the number of grid cells.

<sup>b</sup>Referred to as the 134M simulation, where 134M corresponds to the number of grid cells.

the adiabatic curve on which the initial operating point is lying in the non-dimensional  $p$ - $v$  diagram. The corresponding initial value of the fundamental derivative of gas dynamics is  $\Gamma_{initial} = -0.284$ . During the development of the mixing layer, the thermodynamic conditions stay within a close range around the adiabatic curve as shown in figure 1, because shocklet entropy losses and mechanical dissipation are weak in our case. Also, almost all the thermodynamic states stay within the inversion zone throughout the DG simulation. For air, the same values of reduced specific volume and reduced pressure are selected for the initial thermodynamic state. Critical values used for air are the critical pressure  $p_c = 3.7663 \times 10^6$  Pa and the specific volume  $v_c = 3.13 \times 10^{-3}$  m<sup>3</sup> kg<sup>-1</sup> (Stephan & Laesecke 1985).

The main non-dimensional characteristics of the compressible mixing layer are the convective Mach number (1.3) and the Reynolds number based on the initial momentum thickness  $\delta_{\theta,0}$ :

$$Re_{\delta_{\theta,0}} = \Delta u \delta_{\theta,0} / \nu, \quad (2.1)$$

where  $\nu$  denotes the kinematic viscosity and the momentum thickness at time  $t$  is defined as

$$\delta_{\theta}(t) = \frac{1}{\rho_0 \Delta u^2} \int_{-\infty}^{+\infty} \bar{\rho} \left( \frac{\Delta u^2}{4} - \tilde{u}_x^2 \right) dy, \quad (2.2)$$

with  $\rho_0 = (\rho_1 + \rho_2)/2$  the averaged density and  $\tilde{u}_x$  the Favre averaged streamwise velocity (defined in (2.13)).

The first part of the study aims at validating the present DNS results using the results of Pantano & Sarkar (2002) as reference. Following this reference work, the convective Mach number is set equal to 1.1 as previously mentioned, the initial density ratio between the upper and lower streams is equal to unity and the Reynolds number based on the initial momentum thickness is set equal to 160. Table 2 reports the simulation parameters (domain size, grid resolution, dimensional values of velocity and initial momentum thickness). The ratio  $r$  between the Kolmogorov scale and the cell size is about 0.52 for the least refined mesh (16.8M simulation) during the selected self-similar range (see § 3.1). To check grid convergence and because the value  $r = 0.52$  corresponding to the baseline mesh is not very large for a DNS, a second DNS has been performed with a refined mesh obtained by doubling the number of grid cells in each direction (134M simulation) yielding a ratio  $r$  equal to 1.03. Turbulent scales are adequately resolved since the TKE is very low close to the Kolmogorov scale (Moin & Mahesh 1998).



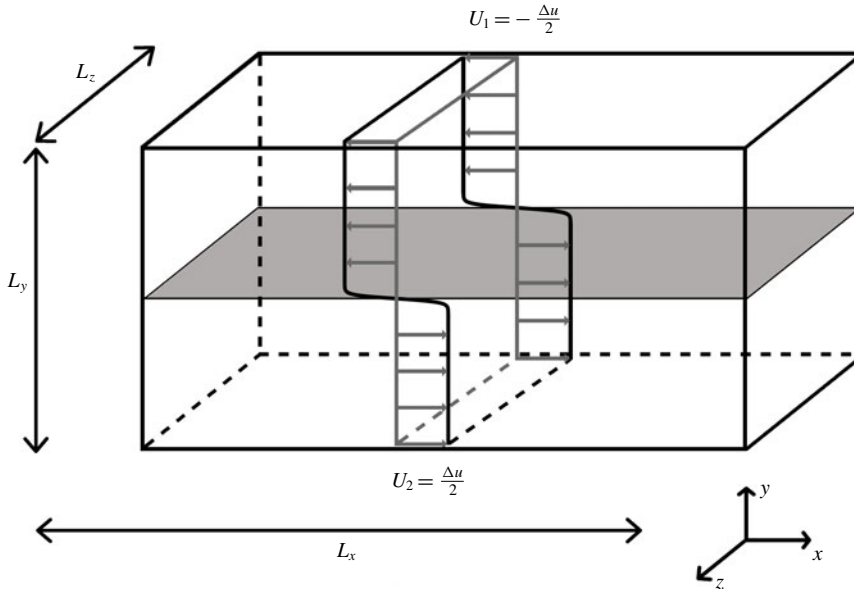


FIGURE 2. Schematic view of the temporal mixing layer configuration. The grey plane represents the initial momentum thickness and its thickness is at scale with the lengths of the computational domain.

In the present study, the temporal mixing layer, less computationally expensive, is chosen instead of the spatial mixing layer. There are slight differences between the two configurations. For the temporal mixing layer, the two streams flow in opposite directions, which enables one to increase the differential speed with a less important absolute speed for each stream (see figure 2). For the spatial mixing layer, both streams flow in the same direction and a speed gap which corresponds to the differential speed is imposed. The transition from one configuration to the other is a change of Galilean reference frame given by (de Bruin 2001)

$$t\Delta u_{temporal} = \frac{x\Delta u_{spatial}}{u_c}, \quad (2.3)$$

where  $t$  denotes the time scale of the temporal configuration,  $\Delta u_{temporal}$  the differential speed of the temporal evolution,  $\Delta u_{spatial}$  the differential speed of the spatial evolution,  $u_c = (U_1 + U_2)/2$  the convective speed and  $x$  the streamwise position scale of the spatial configuration.

The temporal mixing layer requires periodic boundary conditions in the  $x$  and  $z$  directions. A non-reflective boundary condition is imposed in the  $y$  direction to prevent the reflection of acoustic waves inside the computational domain. The NSCBC model proposed by Poinso & Lele (1992) is used.

The mean streamwise velocity is initialized with a hyperbolic tangent profile:

$$\bar{u}_x(y) = \frac{\Delta u}{2} \tanh\left(-\frac{y}{2\delta_{\theta,0}}\right). \quad (2.4)$$

The complete streamwise velocity field is obtained by adding a fluctuating component to the mean component. For the  $y$  and  $z$  components of the velocity,

the mean part is set equal to zero. A Passot–Pouquet spectrum is imposed for the initial velocity fluctuation:

$$E(k) = (k/k_0)^4 \exp(-2(k/k_0)^2), \quad (2.5)$$

where  $k$  denotes the wavenumber. The peak wavenumber  $k_0$  corresponds to the integral scale for which the TKE is maximum inside the initial mixing layer. Peak wavenumber  $k_0$  is set to  $2\pi/(L_x/48)$ . The obtained velocity field is then multiplied by an exponential decay over the  $y$  direction in order to inject turbulent energy in the initial momentum thickness only. That is done in the same way as Pantano & Sarkar (2002):

$$f(y) = \frac{1}{\sigma\sqrt{2\pi}} \exp\left(-\frac{(y-L_y/2)^2}{2\sigma^2}\right), \quad (2.6)$$

where the full width at half maximum of the peak is set equal to the initial momentum thickness  $\delta_{\theta,0} = 2\sigma\sqrt{2\ln(2)}$ . Also, the Gaussian distribution is normalized to reach a maximum value of 1 at the centre  $y=L_y/2$ .

## 2.2. Governing equations

The unsteady, three-dimensional, compressible Navier–Stokes equations are solved to describe the temporally evolving mixing layer:

$$\frac{\partial \rho}{\partial t} + \frac{\partial(\rho u_i)}{\partial x_i} = 0, \quad (2.7)$$

$$\frac{\partial(\rho u_i)}{\partial t} + \frac{\partial(\rho u_i u_j)}{\partial x_j} = -\frac{\partial p}{\partial x_i} + \frac{\partial \tau_{ij}}{\partial x_j}, \quad (2.8)$$

$$\frac{\partial(\rho E)}{\partial t} + \frac{\partial[(\rho E + p)u_j]}{\partial x_j} = \frac{\partial(\tau_{ij}u_i - q_j)}{\partial x_j}, \quad (2.9)$$

where  $\tau_{ij} = \mu((\partial u_i/\partial x_j) + (\partial u_j/\partial x_i) - \frac{2}{3}(\partial u_k/\partial x_k)\delta_{ij})$  denotes the viscous stress tensor ( $\mu$  is the dynamic viscosity),  $E = e + \frac{1}{2}u_i u_i$  the specific total energy ( $e$  is the specific internal energy) and  $q_j = -\lambda(\partial T/\partial x_j)$  the heat flux given by Fourier's law ( $\lambda$  is the thermal conductivity).

For the DG (FC-70), dynamic viscosity and thermal conductivity follow the model proposed by Chung *et al.* (1988). FC-70 is assumed to behave as a non-polar gas so that its dipole moment can be neglected (Shuely 1996). For the PG (air), the dynamic viscosity follows Sutherland's law (Sutherland 1893) and a constant Prandtl number equal to 0.71 is used. The selected constants for Sutherland's law are the ones given by White (1998), which are valid for the range of temperature met in the air mixing layer studied in the present study (Grieser & Goldthwaite 1963).

Equations (2.7)–(2.9) are completed with thermal and calorific EoS. Air is thermodynamically described by the PG EoS:

$$\left. \begin{aligned} p &= \rho RT, \\ e &= e_{ref} + \int_{T_{ref}}^T c_v(T') dT', \end{aligned} \right\} \quad (2.10)$$

where  $R$  is the specific gas constant,  $c_v$  the specific heat capacity,  $p$  the pressure,  $T$  the temperature and  $\rho$  the density.

The specific heat capacity  $c_v$  is defined as the slope of the sensible energy ( $c_v = (\partial e_s / \partial T)|_v$ ). The sensible energy is computed using the JANAF tables (Stull & Prophet 1971). Specific heats are thus not constant and the relation  $\Gamma = (\gamma + 1)/2$  is no longer suitable, since it is only valid for a thermally and calorically PG.

The DG FC-70 is described by the MH EoS (Martin & Hou 1955), as improved by Martin, Kapoor & De Nevers (1959). The MH EoS are given by the following fifth-order equations:

$$\left. \begin{aligned} p &= \frac{RT}{v-b} + \sum_{i=2}^5 \frac{A_i + B_i T + C_i e^{-kT/T_c}}{(v-b)^i}, \\ e &= e_{ref} + \int_{T_{ref}}^T c_v(T') dT' + \sum_{i=2}^5 \frac{A_i + C_i(1 + kT/T_c)e^{-kT/T_c}}{(i-1)(v-b)^{i-1}}, \end{aligned} \right\} \quad (2.11)$$

where  $(.)_{ref}$  denotes a reference state,  $b = v_c(1 - (-31\,883Z_c + 20.533)/15)$ ,  $k = 5.475$  and the coefficients  $A_i$ ,  $B_i$  and  $C_i$  are numerical constants determined by Martin & Hou (1955) and Martin *et al.* (1959) from the physical parameters summarized in table 1.

For the sake of physical analysis, the TKE equation can be derived from the Navier–Stokes equations (2.7)–(2.9). Density, pressure and velocity are each decomposed into a mean and fluctuating component as follows:

$$\left. \begin{aligned} \rho &= \bar{\rho} + \rho', \\ p &= \bar{p} + p', \\ u_i &= \bar{u}_i + u'_i, \end{aligned} \right\} \quad (2.12)$$

where  $\bar{\phi}$  denotes the Reynolds average for a flow variable  $\phi$ , while the Favre average  $\tilde{\phi}$  is defined as

$$\tilde{\phi} = \frac{\overline{\rho\phi}}{\bar{\rho}}. \quad (2.13)$$

The Reynolds fluctuation of  $\phi$  is denoted  $\phi'$  while its Favre fluctuation is denoted  $\phi''$ . Because of the periodic conditions, Reynolds averaging is equivalent to plane averaging along the  $x$  and  $z$  directions. Introducing (2.12) into the instantaneous Navier–Stokes equations, applying the averaging process and combining the resulting equations (see details for instance in Bailly & Comte-Bellot (2003)) allow one to obtain the TKE equation:

$$\begin{aligned} \frac{\partial \bar{\rho}\tilde{k}}{\partial t} + \frac{\partial \bar{\rho}\tilde{k}\bar{u}_j}{\partial x_j} &= \underbrace{-\overline{\rho u'_i u'_j} \frac{\partial \bar{u}_i}{\partial x_j}}_{\text{Production}} - \underbrace{\overline{\tau'_{ij} \frac{\partial u'_i}{\partial x_j}}}_{\text{Dissipation}} \\ &\quad + \underbrace{\frac{1}{2} \frac{\partial \overline{\rho u'_i u'_j u'_k}}{\partial x_j}}_{\text{Turbulent transport}} - \underbrace{\frac{\partial \overline{p' u'_i}}{\partial x_i}}_{\text{Pressure transport}} + \underbrace{\frac{\partial \overline{u'_i \tau'_{ij}}}{\partial x_j}}_{\text{Viscous transport}} \\ &\quad + \underbrace{\overline{p' \frac{\partial u'_i}{\partial x_i}}}_{\text{Pressure dilatation}} - \underbrace{\overline{u'_i \left( \frac{\partial \bar{p}}{\partial x_i} - \frac{\partial \bar{\tau}_{ij}}{\partial x_j} \right)}}_{\text{Mass-flux term}}, \end{aligned} \quad (2.14)$$

where  $\tilde{k} = \frac{1}{2}\widetilde{u_i''u_i''}$  denotes the specific TKE. Equation (2.14) details the physical quantities at stake in a compressible mixing layer, with the production and the dissipation terms being the main terms in this equation. The former depends on the turbulent stress tensor while the latter corresponds to the viscous dissipation. For incompressible configurations, the mass-flux coupling term and the pressure–dilatation term are equal to zero. Also, the dissipation can be decomposed into solenoidal, low-Reynolds-number and dilatational components. This compressible component is related to the occurrence of eddy shocklets and can be written as (Sarkar & Lakshmanan 1991)

$$\epsilon_d = \frac{4}{3}\bar{v}\overline{\left(\frac{\partial u_k''}{\partial x_k}\right)^2}. \quad (2.15)$$

### 2.3. Numerical set-up

The numerical solver AVBP is used to solve the three-dimensional unsteady compressible Navier–Stokes equations (2.7)–(2.9) closed by the EoS (2.10) for air and (2.11) for FC-70. The AVBP solver is massively parallel and designed for LES and DNS (Desoutter *et al.* 2009; Cadieux *et al.* 2012). It is widely used for combustion in industry and allows the numerical resolution of the three-dimensional compressible Navier–Stokes equations using a two-step time-explicit Taylor–Galerkin scheme (TTGC) for the hyperbolic terms based on a cell-vertex formulation (Colin & Rudgyard 2000). The scheme ensures third-order accuracy in space and in time. The order of accuracy of the numerical scheme can be thought of as being low to perform a DNS. That is why refined simulations (134M simulations) have been performed in order to ensure the reliability of the computed flow solutions. The ratio  $r$  between the Kolmogorov scale and the grid cell size ( $L_\eta/\Delta x$ ) is about 1.03 at the centreline during the self-similar period for the PG simulation including 134M elements (see table 3 in appendix A).

## 3. Direct numerical simulation validation for a PG compressible mixing layer

In order to assess the quality of the present DNS, this section is devoted to the assessment of air (considered as a PG) simulations, which will be compared in particular to the available results of Pantano & Sarkar (2002) for exactly the same flow configuration but also with the general trends and correlations available from the analysis of the literature on the compressible turbulent mixing layer.

### 3.1. Temporal evolution and selection of the self-similar period

Figure 3 shows the temporal evolution of the mixing layer momentum thickness computed for the two levels of grid refinement, along with results from the available literature (Pantano & Sarkar 2002; Fu & Li 2006; Martínez Ferrer *et al.* 2017). The time is non-dimensional ( $\tau = t\Delta u/\delta_{\theta,0}$ ) and the momentum thickness is normalized by its initial value. Grid convergence seems well achieved since the mixing layer growth rates are very close between both simulations (16.8M and 134M). Additional proofs of grid convergence are provided in appendix A. The momentum thickness temporal evolution is composed of three main sequences:

- (i) The first one is a kind of delay, observed in the results of Martínez Ferrer *et al.* (2017) and Fu & Li (2006) and in the present results, but which appears rather short in the results of Pantano & Sarkar (2002). This delay is likely to

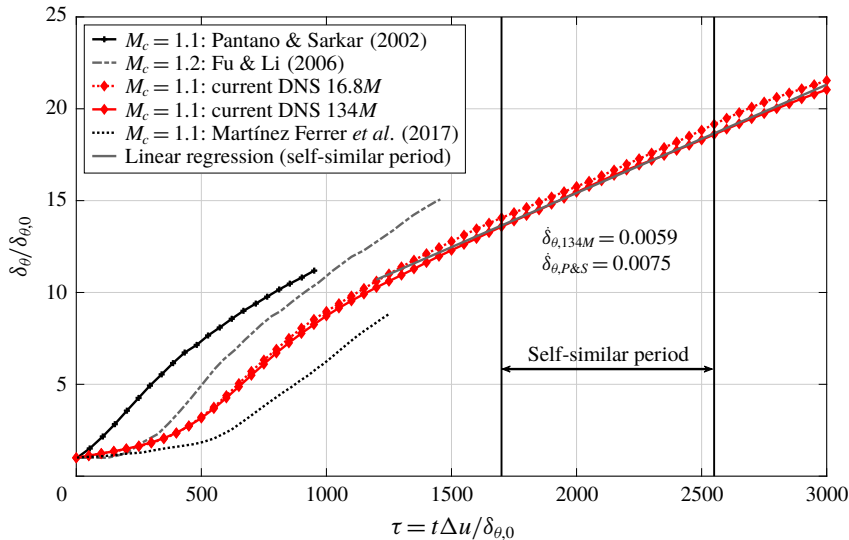


FIGURE 3. Temporal evolution of the mixing layer momentum thickness. Comparison is made between the two different grid precisions (16.8M and 134M grid elements) to check the grid convergence and with the available literature (Pantano & Sarkar 2002; Fu & Li 2006; Martínez Ferrer *et al.* 2017).

be a transition of modes. The energy is initially injected inside the mixing layer through a Passot–Pouquet spectrum with a corresponding integral length set equal to  $L_x/48$ . Afterwards, the energy is distributed over the whole spectrum and some unstable modes are amplified leading to unstable growth.

- (ii) The second step of the development of the mixing layer consists of an unstable growth governed by two modes of instability, a wake mode superposed onto a canonical mixing layer mode (Pirozzoli *et al.* 2015). It eventually turns into an over-linear growth rate.
- (iii) Finally, the system reaches a saturation point. At this time, a self-similar state is developing until the turbulent structures exit the computational domain above and below the mixing layer. Self-similarity is characterized by a linear evolution of the momentum thickness over time.

In order to analyse and average the TKE balance (necessary to assess the contribution of the significant turbulent terms), the flow needs to be in a statistically stable state, which corresponds to self-similarity. The objective of this section is to determine the appropriate self-similar range, which is a quite complex task since criteria to characterize this self-similar period are not precisely defined in the literature.

Barre & Bonnet (2015) define their flow as self-similar when they obtain superposition of the mean velocity profiles. Rogers & Moser (1994) conclude that self-similarity is reached because of the linear evolution of the momentum thickness, the collapse on a single curve of the mean velocity profiles and the collapse on a single curve of the Reynolds stress profiles. However, the determination of the proper superposition of several curves is sometimes difficult and may be subjective. The same remarks apply to the determination of the linear evolution of the momentum thickness. Analysis of data obtained by Pantano & Sarkar (2002), Rogers & Moser

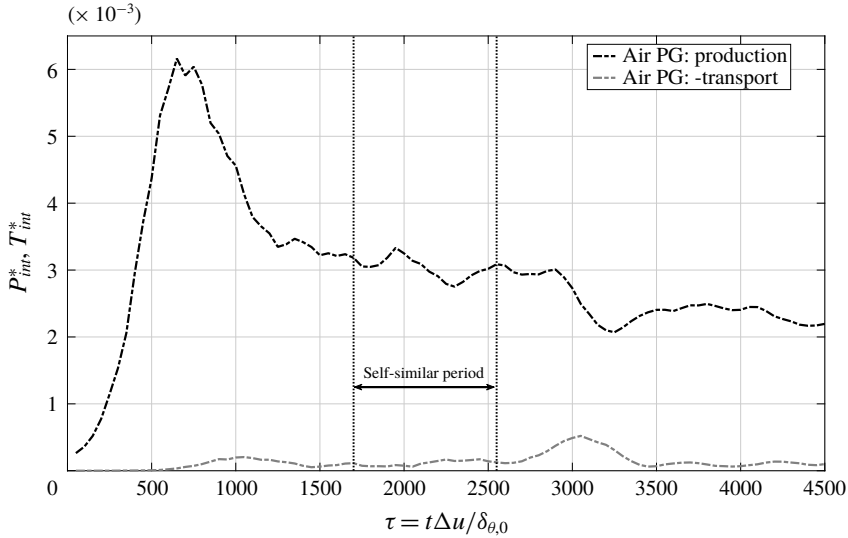


FIGURE 4. Temporal evolution of the non-dimensional streamwise production and the non-dimensional total transport terms integrated over the whole domain, respectively  $P_{int}^* = (1/(\rho_0\Delta u^3)) \int_{L_y} \bar{\rho} P_{xx} dy$  (with  $\bar{\rho} P_{xx} = -\bar{\rho} u_x'' u_y'' (\partial \tilde{u}_x / \partial y)$ ) and  $T_{int}^* = (1/(\rho_0\Delta u^3)) \int_{L_y} (\partial T_k / \partial x_k) dy$  (with  $\partial T_k / \partial x_k = \partial (\frac{1}{2} \bar{\rho} u_i'' u_i'' u_j'' + p' u_i'' - u_i'' \tau_{ij}') / \partial x_k$ ). Results are computed from the 134M simulation.

(1994) and Zhou *et al.* (2012) shows that the growth rate is probably sub-linear, as also stated by Pirozzoli *et al.* (2015). Many authors confirmed the difficulty encountered in reaching a perfect self-similar state (Pantano & Sarkar 2002; Pirozzoli *et al.* 2015). The diversity of results found in the literature for the well-known growth rate versus convective Mach number graph comes in part from this difficulty in accurately defining the growth rate.

Another method to determine self-similarity is used in this study. It consists of computing the streamwise production term integrated over the whole domain. Vreman *et al.* (1996) indeed demonstrate the following relation between the volumetric streamwise production power ( $\bar{\rho} P_{xx} = -\bar{\rho} u_x'' u_y'' (\partial \tilde{u}_x / \partial y)$ ) and the momentum thickness growth rate:

$$\delta'_\theta = \frac{d\delta_\theta}{dt} = \frac{2}{\rho_0 \Delta u^2} \int \bar{\rho} P_{xx} dy. \tag{3.1}$$

From the above, a constant evolution of the integrated volumetric streamwise production power implies a constant growth rate of the mixing layer. Figure 4 displays this production term as well as the total transport term, which comprises the pressure, the turbulent and the viscous contributions. The chosen self-similar period is given on the graph ( $\tau \in [1700; 2550]$ ) and corresponds to a converged state of the mixing layer. A long period has been chosen (about  $900\tau$ ) in comparison with the available literature. Pantano & Sarkar (2002) and Rogers & Moser (1994), respectively, selected in their studies a period of 257 and 45 non-dimensional times.

The temporal evolution of the production is consistent with the temporal evolution of the momentum thickness. The three steps mentioned above can be identified. During unstable growth, the production quickly increases, until it reaches a maximum.



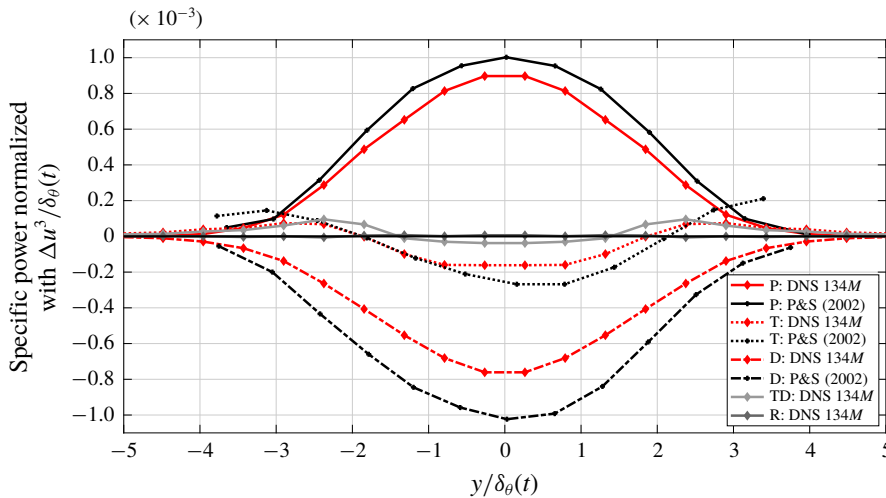


FIGURE 5. Distributions of the normalized specific power quantities over the  $y$  direction are presented for air: P (production), D (dissipation) and T (transport) are normalized by  $\Delta u^3/\delta_\theta(t)$  and compared to results of Pantano & Sarkar (2002). Additional terms (R, residuals; TD, time derivative) are given. The sampling space step of the averaging process is  $(2L_y/\delta_\theta(\tau = 1700))/N_{points}$ , with  $N_{points} = 24$ . Distributions have been averaged between the upper and the lower stream to get perfectly symmetric distributions.

Afterwards, the mixing layer converges to a self-similar state. The chosen self-similar range is also represented in figure 3 and corresponds closely to a linear evolution of the momentum thickness, consistent with figure 4. The computed time evolution of the momentum thickness shows a rather good match with the available literature even though the mixing layer momentum thickness growth rate computed for the current 134M simulation is smaller (a difference of about 20% is observed) than the one of Pantano & Sarkar (2002). Since the computation of the growth rate depends on the chosen self-similar period and since the self-similar period of the current simulation is chosen late enough to achieve a complete convergence, the computed growth rate is smaller. Appendix C provides additional comparisons between PG and DG performed during the selected self-similar period.

### 3.2. Turbulent kinetic energy balance over the selected self-similar period

Once a relevant time interval has been selected to consider the mixing layer to be self-similar, one can focus on the study of the turbulent kinetic power balance. This equation evaluates terms at stake in the development of the turbulence. It also helps to validate our simulation by comparing the present DNS results with those of Pantano & Sarkar (2002). In figure 5, quantities are integrated over the two periodic directions ( $x$  and  $z$ ), normalized by  $\Delta u^3/\delta_\theta(t)$  and drawn versus the non-dimensional cross-stream direction  $y/\delta_\theta(t)$ . Solutions are averaged over time in the self-similar range ( $\tau \in [1700; 2550]$ ).

The present DNS results agree reasonably well, especially the production and the transport terms, with the results of Pantano & Sarkar (2002): shape as well as intensity are close. The gap between the dissipation terms could be explained by the difference in the choice for the self-similar period. Since the dissipation is linked with

the velocity fluctuation gradient and since this last quantity decreases after unstable growth, if the self-similar period is chosen at a earlier time, the dissipation power gets closer to the term of Pantano & Sarkar (2002).

The two additional quantities are the residuals and the time derivative of the TKE. Residuals are almost zero and thus attest to the proper closure of the balance. The time derivative is far from being negligible and has almost the same intensity as the transport term. This term is rarely reported in the literature possibly because of difficulties encountered when extracting it, especially for the temporal mixing layer. Also, the convective derivative is negligible, in contrast with Zhou *et al.* (2012) who studied a spatial mixing layer. In fact, the time derivative of the kinetic energy in a temporal mixing layer and the convective derivative of the kinetic energy in a spatial mixing layer play a symmetric role since the two configurations are linked by a change of Galilean reference frame. It is thus expected that the time derivative in the temporal mixing layer is non-negligible in the same way that the convective derivative in the spatial mixing layer is significant. Finally, it has been noticed that the compressible dissipation, the pressure dilatation, the mass-flux coupling term including the velocity pressure gradient and the convective derivative are negligible in the present study and are thus not represented. Similar observations have been consistently made by several authors to support this fact as previously mentioned in the introduction.

### 3.3. Validation of the specific TKE spectrum

The TKE balance computed over the whole range of turbulent scales is not the only tool available to highlight the influence of the main terms of the TKE equation. Spectra are very useful to compare TKE scale by scale. In the next section, devoted to the comparison between PG and DG simulations, a comparison at each turbulent scale will be performed through a comparison of the respective PG and DG flow spectra. At this stage, the authors wish to validate the spectrum computed for air. To this end, the present DNS results are compared with those of the current literature in figure 6 (Freund *et al.* 2000; Tanahashi, Iwase & Miyauchi 2001; Okong'o & Bellan 2002; Pantano & Sarkar 2002). The current spectrum is computed over the centreline and averaged over the self-similar period ( $\tau \in [1700; 2550]$ ). Because the spectra from the literature display different large-scale values, they are normalized by their value at  $10k_0$ . This value is indeed a good threshold to compare spectra at small scales without being subjected to geometry differences. The present results are found to compare favourably with the current literature and the expected reference slopes. The  $-7$  slope in the logarithmic scale has been established by Batchelor (1953) to describe the evolution of kinetic energy at small scales and is consistent with the present spectrum at high wavenumber range. This indicates a proper resolution of the small scales. The  $-5/3$  and  $-2$  slopes are the slopes of isothermal homogeneous isotropic turbulence inertial ranges, respectively, for incompressible and compressible flows (Kritsuk *et al.* 2007).

The accuracy of the present PG DNS having been established by comparison with available results from the literature, we can now proceed to compare the novel DG (FC-70) flow computations with the results for air in order to identify the potential specificities of DG turbulence.

## 4. Comparison between PG and DG

### 4.1. Temporal evolution and selection of the self-similar period

As done for the PG validation process, the computation of the TKE balance requires first the selection of the self-similar range. This is achieved through a combined

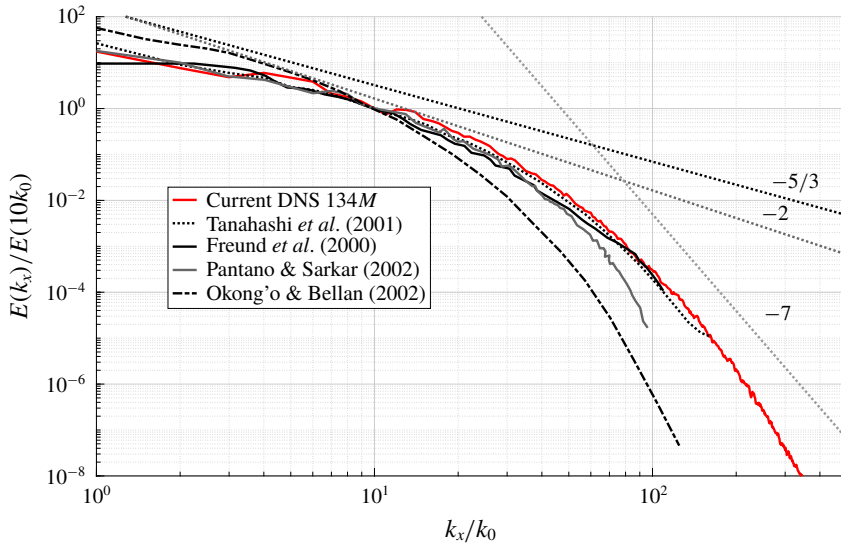


FIGURE 6. Streamwise specific TKE spectra computed over the centreline. Comparison is made with the available literature.

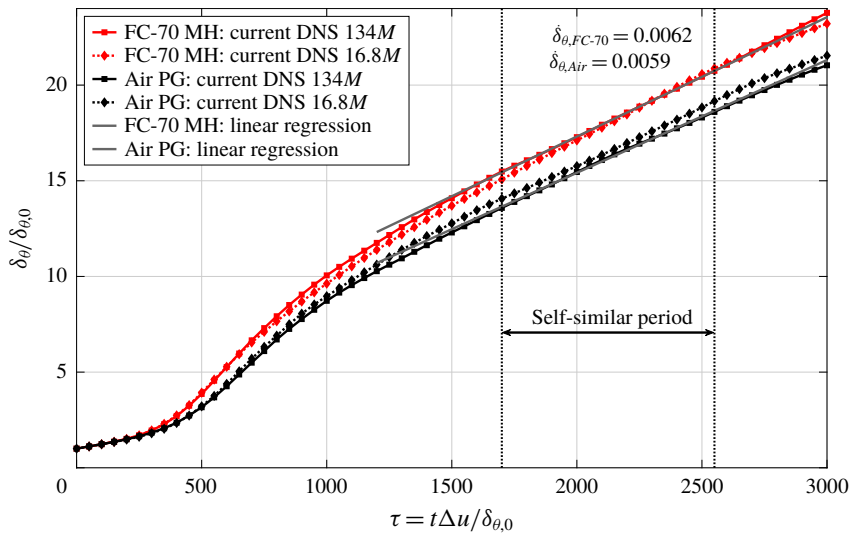


FIGURE 7. Temporal evolution of the mixing layer momentum thickness.

investigation of the momentum thickness evolution and the evolution of the integrated production and transport terms over time. Figure 7 displays the momentum thickness temporal evolution: PG and DG results show a similar evolution. The curves are initially ( $\tau \leq 200$ ) very close, with a different evolution for PG and DG mixing layers taking place in the second step of the mixing layer development (approximately  $200 \leq \tau \leq 1500$ ), when the unstable growth is governed by instability modes. The DG unstable growth is faster than the PG one, likely because instability modes and their amplification factor evolve differently for PG and DG mixing layers. Figure 7

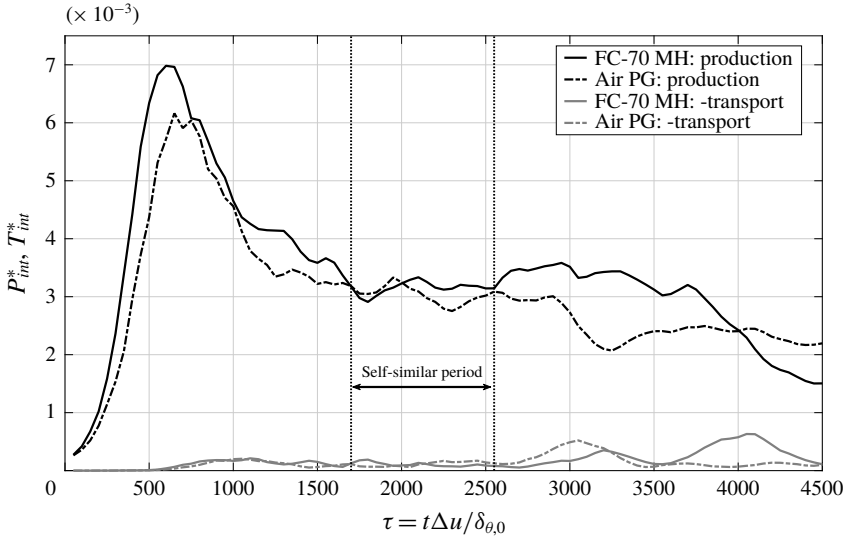


FIGURE 8. Temporal evolution of the non-dimensional streamwise production and the non-dimensional total transport terms integrated over the whole domain, respectively  $P_{int}^* = (1/(\rho_0 \Delta u^3)) \int_{L_y} \bar{\rho} P_{xx} dy$  (with  $\bar{\rho} P_{xx} = -\bar{\rho} u'_x u''_y (\partial \bar{u}_x / \partial y)$ ) and  $T_{int}^* = (1/(\rho_0 \Delta u^3)) \int_{L_y} (\partial T_k / \partial x_k) dy$  (with  $\partial T_k / \partial x_k = \partial (\frac{1}{2} \bar{\rho} u'_i u''_i u''_j + p' u'_i - u'_i \tau'_{ij}) / \partial x_k$ ). Results are computed from the 134M simulation.

also displays the evolution of the DG momentum thickness for the 16.8M simulation, which is very close to the 134M simulation, demonstrating grid convergence.

Figure 8 displays the integrated production and transport terms. The DG turbulent production is found to be larger than the PG production, consistent with the larger DG momentum thickness growth rate. Although the unstable evolution is faster for the DG mixing layer, both mixing layers reach a self-similar stage almost at the same time as confirmed in figure 8. The growth rate slopes calculated during the self-similar stage are reported in figure 7: the slope is slightly larger for the DG than for the PG with a typical 5% difference between DG and PG mixing layers.

The evolution of the integrated transport term provides information on exit flux from the computational domain. It seems that the DG mixing layer displays an extended converged self-similar state compared with the PG mixing layer. The choice has, however, been made in the current study to select a common self-similar range, namely  $\tau \in [1700; 2550]$ .

From the above analysis, the comparison between the DG and the PG mixing layers can be divided into two main parts: the initial unstable growth, where differences between the two mixing layers are significant; and the self-similar range, where the dynamics of the mixing layers seem rather close.

#### 4.2. Unstable growth analysis

During the unstable growth, the momentum thickness evolution is governed by instability modes and their amplification mechanism. A larger growth is directly related to a larger production term according to Vreman *et al.* (1996). The streamwise production term is composed of the Favre averaged velocity gradient and the turbulent

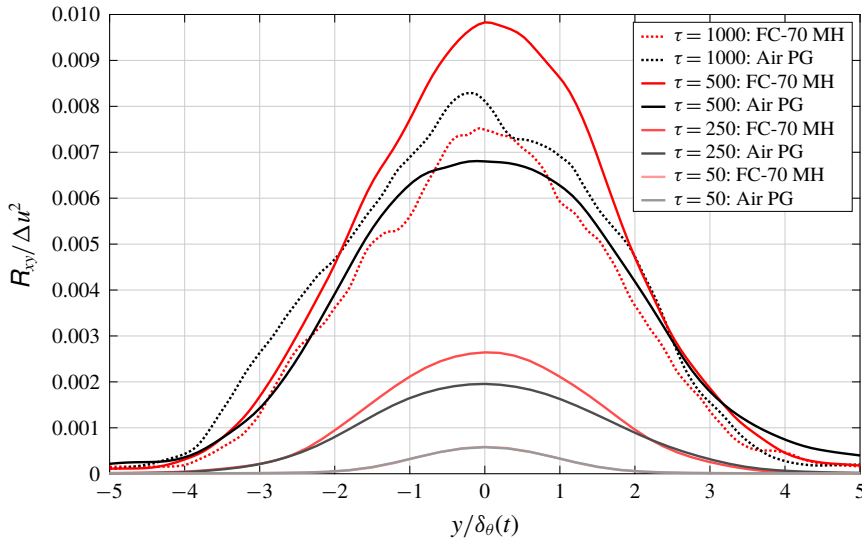


FIGURE 9. Distribution of the  $xy$  component of the turbulent stress tensor ( $R_{xy} = \overline{\rho u'_x u'_y} / \bar{\rho}$ ) over the non-dimensional direction  $y/\delta_\theta(t)$ . Results are computed from the 134M simulation. The curves for FC-70 and air at  $\tau = 50$  collapse.

stress tensor. The comparison of the first term does not show significant differences between DG and PG unlike the second term. Figure 9 displays the distributions of the  $xy$  component of the turbulent stress tensor  $R_{xy} = \overline{\rho u'_x u'_y} / \bar{\rho}$  normalized by  $\Delta u^2$  over the normalized cross-stream direction  $y/\delta_\theta(t)$  during the initial growth. The DG  $xy$  component of the turbulent stress tensor increases much faster than the PG one until  $\tau \approx 500$ . Afterwards, both tensors reach the same level at  $\tau \approx 1000$ . This observation is consistent with the temporal evolution of the integrated streamwise production term.

In order to better understand the difference of dynamics between PG and DG, the comparison of PG and DG mixing layers during the unstable growth is investigated using the specific TKE spectra. Spectra reported in figure 10 are computed on the centreline in the streamwise direction. One can notice the sudden increase of the specific TKE at the smallest scales for the DG. Consistent with observations made by the authors for DNS of forced HIT (Vadrot, Giauque & Corre 2019) in a DG, the dynamics at the smallest scales is different between the PG and DG. The slope of the specific TKE decrease at the smallest scales tends to be larger for the DG in comparison with the PG.

This increase is not likely to explain the different unstable growth phase between DG and PG because this region of the spectrum corresponds to low-energy modes. However, in the approximate range  $k_x/k_0 \in [10; 22]$ , energy is much larger for the DG when compared to the PG (a factor of between 2 and 3 is found). These modes are high-energy modes and are responsible for the difference between the DG and the PG during the unstable growth phase.

Another explanation can be found in the evolution of the turbulent Mach number  $M_t$ , displayed in figure 11 for FC-70 and air. The turbulent Mach number is computed

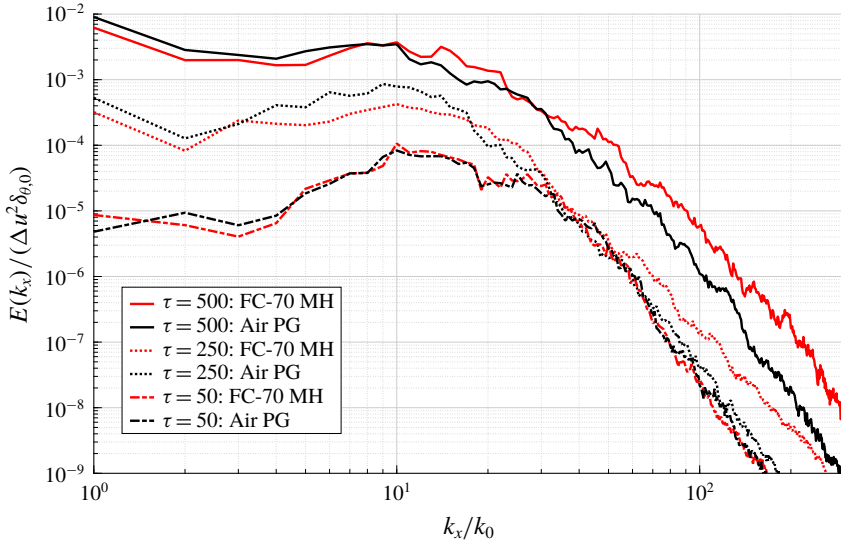


FIGURE 10. Specific TKE spectra in the streamwise direction computed over the centreline during the unstable growth phase. Results are computed from the 134M simulation.

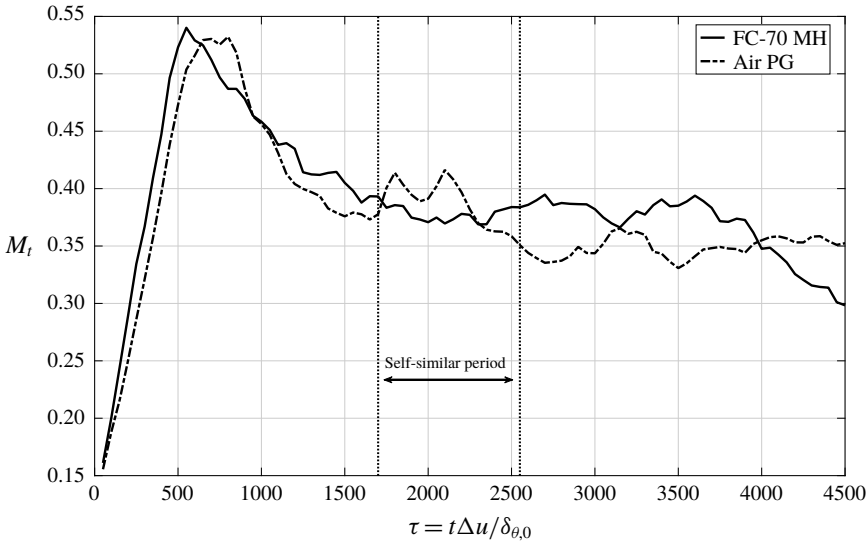


FIGURE 11. Temporal evolution of turbulent Mach number. Results are computed from the 134M simulation.

using the following relation:

$$M_t = \frac{\sqrt{\overline{u_x^2} + \overline{u_y^2} + \overline{u_z^2}}}{c}. \tag{4.1}$$



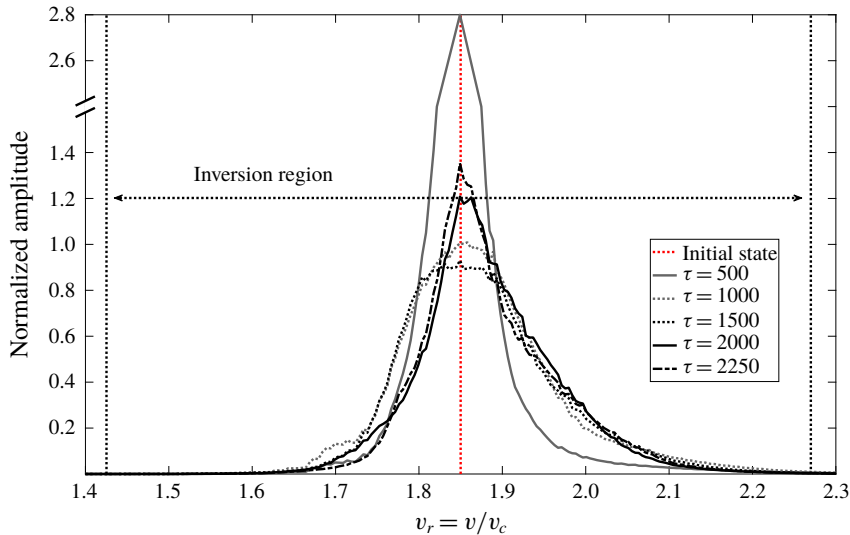


FIGURE 12. Distribution of thermodynamic states along the initial adiabetic curve. Amplitude is normalized with the maximum value at  $\tau = 1000$ . Results are computed from the 134M simulation.

Turbulent Mach numbers increase during the unstable growth phase until  $M_t \approx 0.53$ . Evolutions for DG and PG are very close during this first phase, with a slightly larger value for the DG, which is consistent with the evolutions of the turbulent production (figure 8). Next, turbulent Mach numbers decrease and reach an approximately constant value during the self-similar period. Average values are almost equal for DG and PG ( $M_{t_{av,DG}} \approx 0.38 < M_{t_{av,PG}} \approx 0.39$ ). Shocklets might be observed during a short period of time during the unstable growth phase ( $\tau \in [500; 750]$ ), which corresponds to the period of time during which discrepancies appears between DG and PG (see figure 7). During this short period of time, even though the values of the turbulent Mach number are almost the same for DG and PG, their effect on the mixing layer growth is different. Since the majority of the thermodynamic states lie inside the inversion region, expansion shocklets could be one reason for the discrepancy between DG and PG. However, since it represents a very short period of time after which  $M_t$  decreases well below the range of values for which shocklets are expected, it is not likely to influence the self-similar period.

#### 4.3. Turbulent kinetic energy balance computed over the self-similar period

Before analysing the TKE equation, it can be checked, in order to maximize the differences between DG and PG, that the DG mixing layer thermodynamic states stay inside the inversion region in the  $p$ - $v$  diagram. Figure 12 presents the thermodynamic state distributions on the adiabetic curve normalized by the maximum value at  $\tau = 1000$ . One can note that almost all the thermodynamic states stay inside the inversion region all along the development of the mixing layer. Also, the distributions seem to become asymmetric towards larger reduced molar volumes ( $v_r$ ) which corresponds to a decrease of the reduced pressures ( $p_r$ ) in figure 1.

During the self-similar period ( $\tau \in [1700; 2550]$ ), both DG and PG mixing layers are in a statistically stable state and the terms of the TKE equation can be averaged.

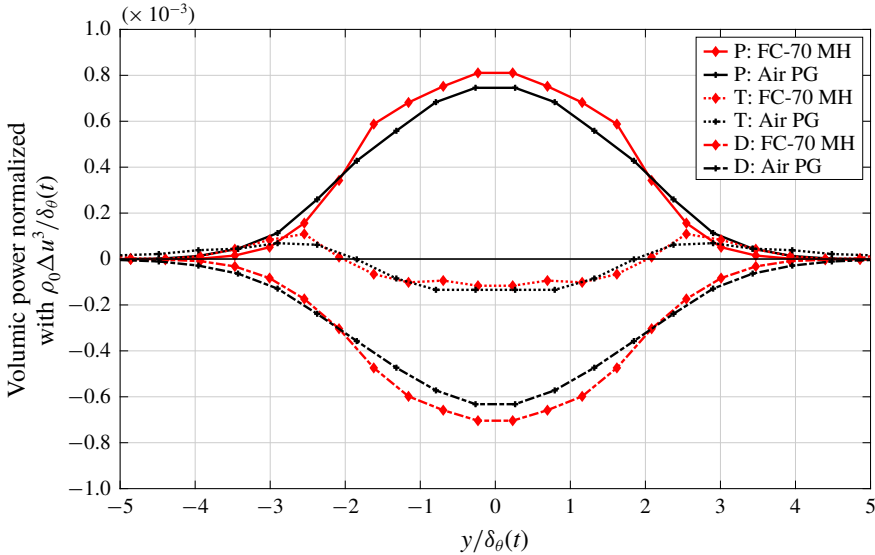


FIGURE 13. Distribution of the volumetric normalized powers over the non-dimensional cross-stream direction  $y/\delta_\theta(t)$ . Here P (production), D (dissipation) and T (transport) are normalized by  $\rho_0 \Delta u^3 / \delta_\theta(t)$ . Results are computed from the 134M simulation. The sampling space step of the averaging process is  $(2L_y / \delta_\theta(\tau = 1700)) / N_{points}$ , with  $N_{points} = 24$ . Distributions have been averaged between the upper and the lower stream to get perfectly symmetric distributions.

Consistent with the evolution of the integrated production given in figure 8 and with the formulation of Vreman *et al.* (1996), powers given in figure 13 are volumetric unlike in figure 5 showing the comparison with Pantano & Sarkar (2002). The choice of using the volumetric or the specific power formulation influences the comparison between DG and PG. The difference between the two formulations can be more easily expressed by a normalization with either  $\rho_0$  or  $\bar{\rho}$ , respectively, for the volumetric and for the specific powers. For the DG, the difference between both formulations is reduced compared with the PG. The decrease of the Reynolds-averaged density over the  $y$  direction is indeed lower for the DG than for the PG. It is likely that the molecular complexity of the DG reduces the temperature increase related to the viscous dissipation, which also reduces the density decrease and thus the difference between the volumetric and specific power formulations (see thermodynamic analysis in appendix B).

Figure 13 shows the comparison of the main volumetric TKE budget terms between the PG and the DG mixing layers. Results are close between the two types of gases. The production term is slightly larger for the DG when compared to the PG, which is consistent with figure 8 and with the 5% increase of the momentum growth rate. The dissipation is also larger for the DG in order to counterbalance the turbulent production. The transport term is almost identical between DG and PG. The pressure transport and turbulent transport terms are close between the two types of gases (the viscous transport is negligible). The DG seems to have a limited effect on these turbulent quantities. However, one can highlight a slower propagation of the TKE terms at the boundaries of the mixing layer as a visible effect induced by the DG: the curves are indeed widened for the PG with respect to the DG. The observation

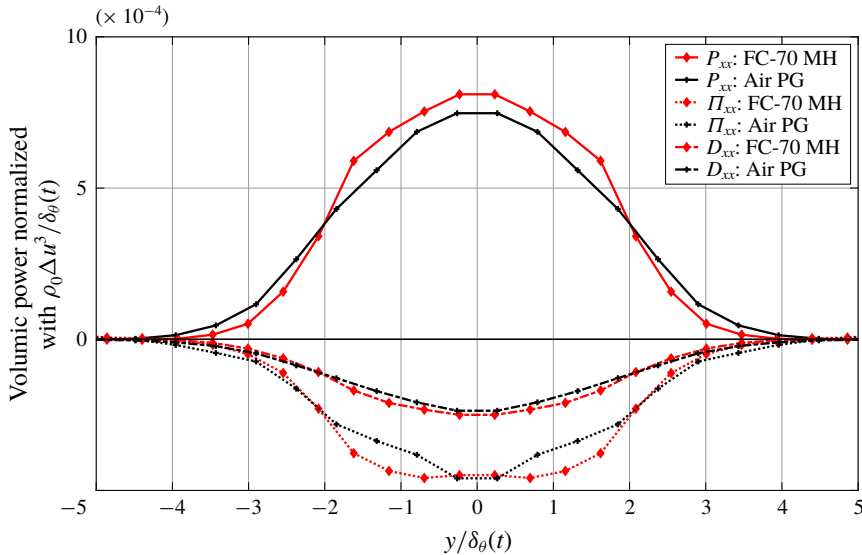


FIGURE 14. Distribution of the main non-dimensional volumetric power terms of the  $x$  turbulent stress tensor ( $\mathcal{R}_{xx}$ ) equation over the non-dimensional cross-stream direction  $y/\delta_\theta(t)$ . The  $P_{xx}$  (streamwise production),  $\Pi_{xx}$  (streamwise pressure–strain) and  $D_{xx}$  (streamwise dissipation) terms are normalized by  $\rho_0 \Delta u^3 / \delta_\theta(t)$ . Results are computed from the 134M simulation. The sampling space step of the averaging process is  $(2L_y / \delta_\theta(\tau = 1700)) / N_{points}$ , with  $N_{points} = 24$ . Distributions have been averaged between the upper and the lower stream to get perfectly symmetric distributions.

of this effect is confirmed by the distributions of mean axial velocity profiles given in figure 26.

Concerning the other terms of the TKE equation, it is found that the compressible dissipation, the pressure dilatation, the mass-flux coupling term and the convective derivative of the TKE are negligible for both PG and DG. Residuals and time derivative agree well between both gases.

As mentioned in the introduction, the well-known compressibility-related reduction of the momentum thickness growth rate is explained by a reduction of the pressure–strain terms ( $\Pi_{ij}$ ). These terms only appear explicitly in the turbulent stress tensor equations. Figures 14 and 15 give the turbulent stress tensor budget terms over, respectively, the  $x$  and  $y$  directions. In the same way as for the PG, the pressure–strain terms are not negligible for the DG, but no significant difference is observed between the DG and the PG. The DG mixing layer seems to suffer the same reduction of the pressure–strain terms as the Mach number increases, which is due to both (i) the reduction of the pressure fluctuations and (ii) the reduction of the gradient of velocity fluctuations when the convective Mach number increases.

At  $y/\delta_\theta(t) = 0$ , a non-monotonic behaviour is observed for DG, which is due to the difference in thermodynamic behaviour illustrated in figure 23. The density fluctuations are indeed larger at the centre of the mixing layer for DG, unlike PG where peaks of root-mean-square density are located at the borders of the layer. This higher density fluctuation rate at the centre is likely to disturb the distributions of production since this term is calculated using Favre averaging.

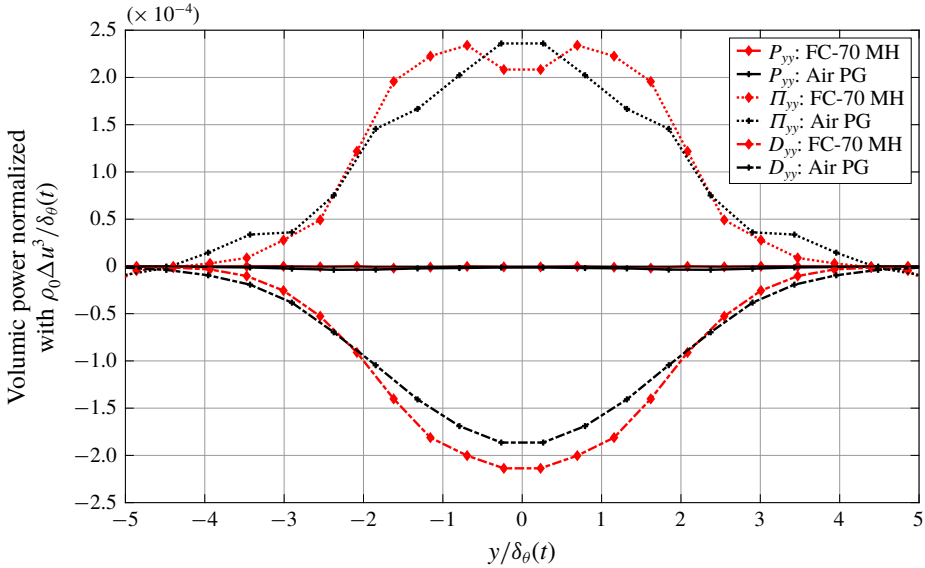


FIGURE 15. Distribution of the main non-dimensional volumetric power terms of the  $y$  turbulent stress tensor ( $R_{yy}$ ) equation over the non-dimensional cross-stream direction  $y/\delta_\theta(t)$ . The  $P_{yy}$  (cross-stream production),  $\Pi_{yy}$  (cross-stream pressure–strain) and  $D_{yy}$  (cross-stream dissipation) terms are normalized by  $\rho_0 \Delta u^3 / \delta_\theta(t)$ . Results are computed from the 134M simulation. The sampling space step of the averaging process is  $(2L_y / \delta_\theta(\tau = 1700) / N_{points})$ , with  $N_{points} = 24$ . Distributions have been averaged between the upper and the lower stream to get perfectly symmetric distributions.

In the vertical direction, production terms are even more non-monotonic for both DG and PG (figure 15) because they involve the vertical gradient of the mean vertical velocity. Since this gradient is calculated in the vertical direction, which corresponds to the direction of the mixing layer growth, it induces much noisier distributions.

#### 4.4. Specific TKE spectra computed during the self-similar period

The aforementioned results do not exhibit significant differences between DG and PG, but that does not imply that there is no difference at all: a turbulent quantity may appear to be the same for PG and DG when looked at as a global quantity over the whole wavenumber range but may actually behave differently at some specific turbulent scales. Since our final objective is to assess the need for new LES subgrid models in the case of turbulent DG flows, it is important to take a closer look at each quantity in the spectral domain. The streamwise specific TKE spectra computed on the centreline are thus shown in figure 16 for DG and PG. Spectra are normalized by  $\Delta u^2 \delta_\theta(t)$  following Pirozzoli *et al.* (2015). The longitudinal Taylor microscale  $\lambda_x$  is also reported in figure 16, computed as (see Bailly & Comte-Bellot 2003)

$$\lambda_x = \sqrt{\frac{2\overline{u_x'^2}}{\left(\frac{\partial \overline{u_x'}}{\partial x}\right)^2}}. \tag{4.2}$$

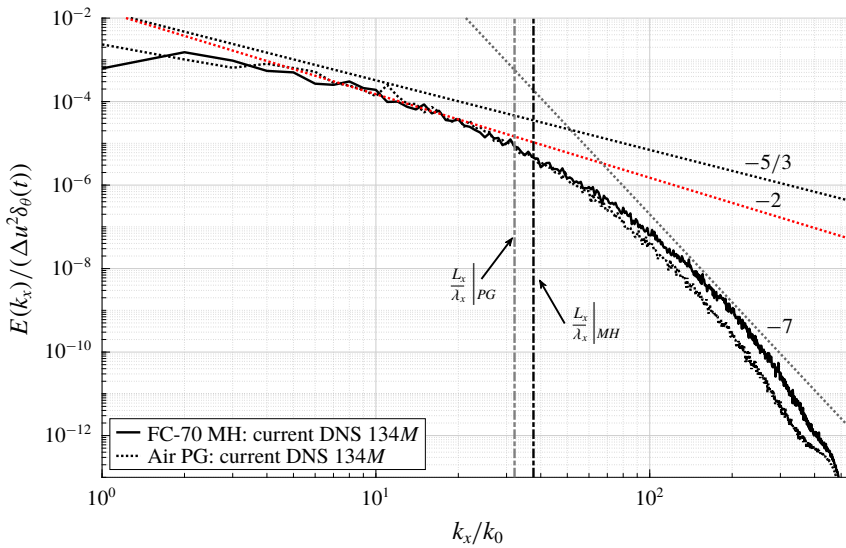


FIGURE 16. Streamwise specific TKE spectra computed on the centreline.

Note that the following simplified equation often used in the literature:

$$\lambda_x = \sqrt{\frac{30\nu u^2}{\epsilon}} \tag{4.3}$$

does not apply here since it is only valid for incompressible and homogeneous turbulence (Kolmogorov 1941).

The evolution of TKE is similar for both PG and DG flows at the largest scales. However, at small scales, the PG TKE is decreasing faster than the DG TKE, an observation reminiscent of the one made for the unstable growth phase. The DG effect therefore seems to increase small-scale energy. The dissipation term, which is the main term at these scales, seems to be reduced. Figure 17 displays the ratio of the DG to the PG spectra and enables one to precisely focus on quantities at stake. At scales smaller than the Taylor microscale, the DG to PG energy ratio increases up to a factor of six.

Note that the  $L_x/\lambda_x$  ratio is slightly smaller for the DG. The turbulent structures at which dissipation plays an important role are smaller for the DG than for the PG.

#### 4.5. Filtered kinetic energy equation computed over the self-similar period

The analysis of the filtered kinetic energy equation balance, developed for compressible flows by Aluie (2013), is of interest in turbulence modelling because it enables one to obtain the main terms at each scale in the spectrum. This approach has only been applied so far to HIT (Wang *et al.* 2018). To the best of the authors' knowledge, no such analysis has been yet conducted for compressible mixing layers. It consists of using a scale decomposition similar to the Favre filtering:

$$\tilde{f}_l = \frac{\overline{\rho f_l}}{\overline{\rho_l}}. \tag{4.4}$$

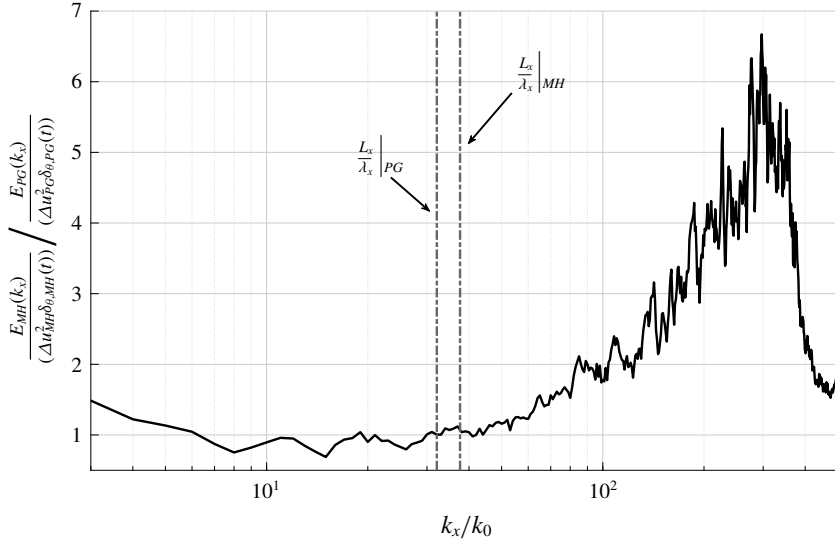


FIGURE 17. Dense gas/perfect gas streamwise specific TKE spectra ratio. Results are computed from the 134M simulation.

Quantities at scales below the filtering scale  $l$  are filtered. The resulting filtered equations for the density and the momentum remain almost unchanged. The only difference is the appearance of the SGS stress tensor  $\bar{\rho}\tilde{t}_{ij} = \bar{\rho}(\widetilde{u_i u_j} - \tilde{u}_i \tilde{u}_j)$ :

$$\frac{\partial \bar{\rho}}{\partial t} + \frac{\partial \bar{\rho}\tilde{u}_i}{\partial x_i} = 0, \tag{4.5}$$

$$\frac{\partial \bar{\rho}\tilde{u}_i}{\partial t} + \frac{\partial \bar{\rho}\tilde{u}_i \tilde{u}_j}{\partial x_j} = -\frac{\partial \bar{p}}{\partial x_i} + \frac{\partial (\bar{\tau}_{ij} - \bar{\rho}\tilde{t}_{ij})}{\partial x_j}. \tag{4.6}$$

The filtered equation for the large-scale kinetic energy is obtained from (4.6):

$$\frac{\partial}{\partial t} \left( \frac{1}{2} \bar{\rho}\tilde{u}_i^2 \right) + J_l = -\Phi_l - \Pi_l - D_l, \tag{4.7}$$

where  $J_l$  represents the transport term,  $\Phi_l$  is the large-scale pressure–dilatation term,  $\Pi_l$  is the SGS kinetic energy flux and  $D_l$  is the viscous dissipation term (using the notations of Wang *et al.* (2018)):

$$J_l = \frac{\partial}{\partial x_j} \left( \frac{1}{2} \bar{\rho}\tilde{u}_i^2 \tilde{u}_j + \bar{p}\tilde{u}_j + \bar{\rho}\tilde{t}_{ij}\tilde{u}_i - \tilde{u}_i \bar{\tau}_{ij} \right), \tag{4.8}$$

$$\Phi_l = -\bar{p} \frac{\partial \tilde{u}_i}{\partial x_i}, \tag{4.9}$$

$$\Pi_l = -\bar{\rho}\tilde{t}_{ij} \frac{\partial \tilde{u}_i}{\partial x_j}, \tag{4.10}$$

$$D_l = \bar{\tau}_{ij} \frac{\partial \tilde{u}_i}{\partial x_j}. \tag{4.11}$$



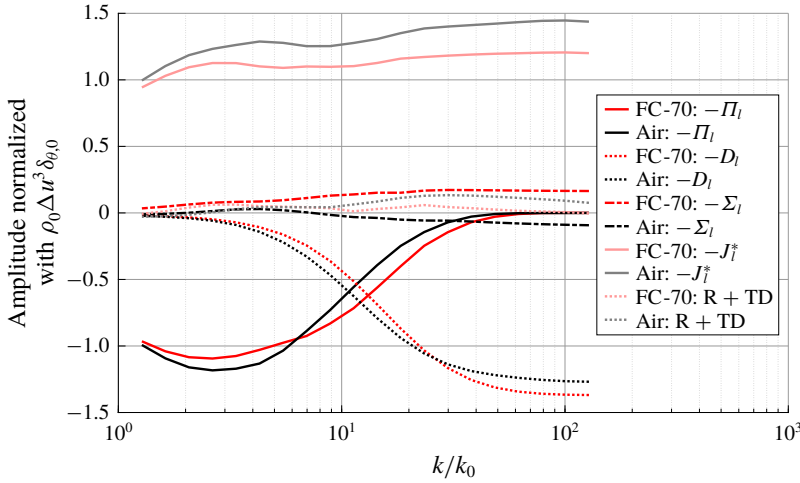


FIGURE 18. Filtered kinetic energy equation terms computed on the centreline of the mixing layer and averaged during the self-similar period ( $\tau \in [1700; 2550]$ ) (R, residuals; TD, time derivative). Results are computed from the 134M simulation.

The ensemble average can be next applied to (4.7) to yield

$$\left\langle \frac{\partial}{\partial t} \left( \frac{1}{2} \bar{\rho} \tilde{u}_i^2 \right) \right\rangle + \langle J_l \rangle = -\langle \Phi_l \rangle - \langle \Pi_l \rangle - \langle D_l \rangle. \tag{4.12}$$

In the mixing layer under study, turbulence is homogeneous along the  $x$  and  $z$  directions. Terms of (4.7) can thus be integrated along these two directions. As previously done for figure 13, the filtered kinetic energy equation is obtained along the mixing layer developing direction ( $y$ ). Unlike HIT, the transport term integrated over the  $x$  and  $z$  directions is not equal to zero. The turbulence is indeed not homogeneous along the  $y$  direction and the boundary conditions are not periodic; it thus cannot be averaged along the transverse direction  $y$ .

Also, the kinetic energy equation terms defined by Wang *et al.* (2018) do not seem fully suitable to study the compressible mixing layer. The large-scale pressure–dilatation term ( $\Phi_l$ ) and the large-scale pressure–transport term ( $\partial(\bar{\rho}\tilde{u}_j)/\partial x_j$ ) exchange energy together and evolve significantly within the wavenumber range and from one integration plane to another. A more appropriate quantity seems to be  $\Sigma_l$  corresponding to the sum of these two terms, which leads to a transformed (with respect to (4.12)) averaged kinetic energy equation:

$$\left\langle \frac{\partial}{\partial t} \left( \frac{1}{2} \bar{\rho} \tilde{u}_i^2 \right) \right\rangle + \langle J_l^* \rangle = -\langle \Sigma_l \rangle - \langle \Pi_l \rangle - \langle D_l \rangle, \tag{4.13}$$

$$J_l^* = \frac{\partial}{\partial x_j} \left( \frac{1}{2} \bar{\rho} \tilde{u}_i^2 \tilde{u}_j + \bar{\rho} \tilde{t}_{ij} \tilde{u}_i - \tilde{u}_i \bar{\tau}_{ij} \right), \tag{4.14}$$

$$\Sigma_l = \tilde{u}_i \frac{\partial \bar{p}}{\partial x_i}, \tag{4.15}$$

where  $\Sigma_l$  represents the power of the pressure strengths computed from the filtered variables. Figure 18 displays the terms of the filtered kinetic energy equation (4.13) computed on the centreline of the mixing layer.

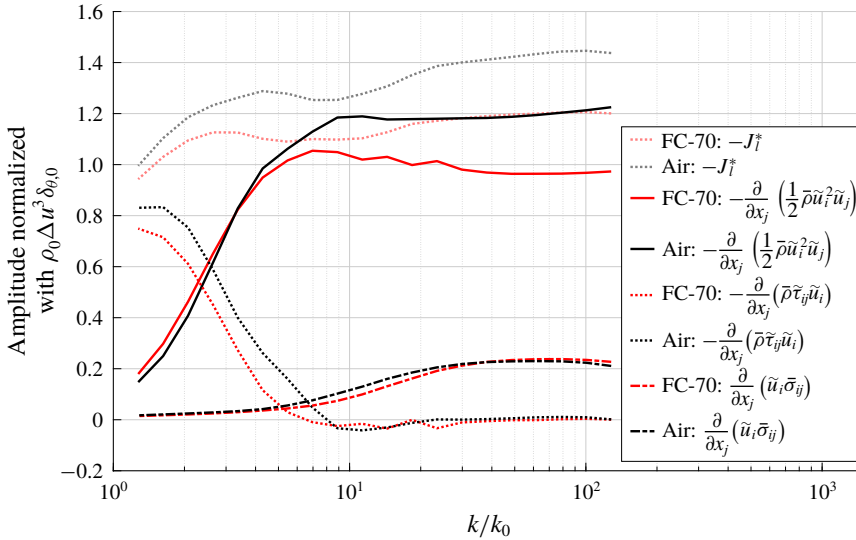


FIGURE 19. Filtered transport terms composing  $J_l^*$  computed on the centreline of the mixing layer and averaged during the self-similar period ( $\tau \in [1700; 2550]$ ). Results are computed from the 134M simulation.

As expected, the SGS kinetic energy flux ( $\Pi_l$ ) prevails at large scales and decreases as the filtering wavelength gets smaller. Unlike the SGS kinetic energy flux, the viscous dissipation ( $D_l$ ) increases with the filtering wavenumber. These two terms are counterbalanced by the transport term. The detailed decomposition of this last term is given in figure 19. The residuals show a good closure of the balance for both types of gases and mostly correspond to the temporal derivative of the TKE.

The comparison between the DG and the PG shows that the transition between the large and small scales, identified by the intersection between the SGS kinetic energy flux and the viscous dissipation term curves, is delayed to higher wavenumbers for the DG when compared to the PG. This observation is consistent with the computed value of the Taylor microscale given in figure 16. Also, the SGS kinetic energy flux seems to be smaller at large scales for the DG when compared to the PG.

A detailed description of the quantities composing the transport term is given in figure 19. One can note that at small scales, the transport term is mainly composed of the convective flux of the filtered kinetic energy ( $-\partial(\frac{1}{2} \tilde{\rho} \tilde{u}_i^2 \tilde{u}_j)/\partial x_j$ ). At large scales, this quantity decreases and the SGS kinetic energy transport term becomes the main term.

Comparison between DG and PG shows that the main quantities are significantly weaker for DG, consistent with figure 18.

### 5. Concluding remarks

Direct numerical simulations of the compressible mixing layer at convective Mach number  $M_c = 1.1$  have been achieved for air described as a PG and FC-70 (BZT gas) described using MH EoS. Perfect gas results have been compared with available results from the literature in order to demonstrate the quality of the present DNS results before moving to the PG versus DG comparison and the identification of DG turbulence specificities. Two sets of observations have been proposed and are summarized here: the first set deals with the general study of compressible mixing

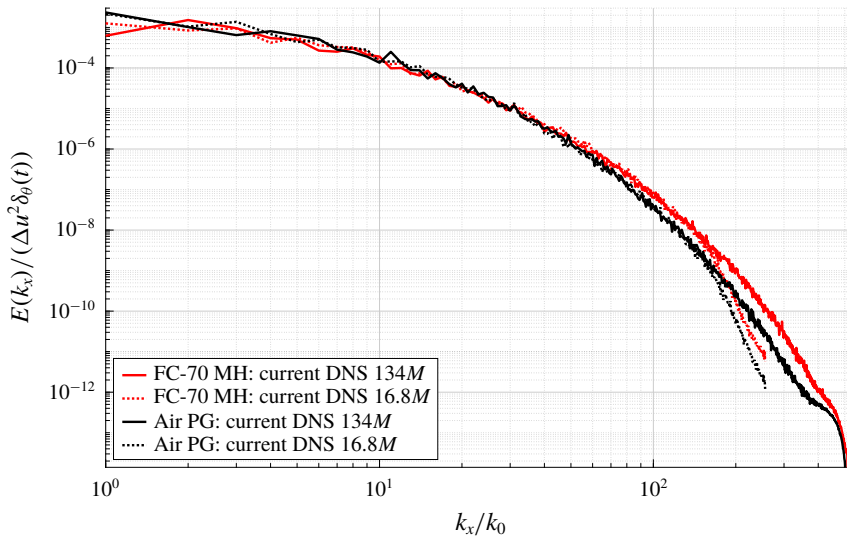


FIGURE 20. Streamwise specific TKE spectra computed on the centreline.

layers while the second set is specific to the DG flow and its comparison to the PG model.

The selection of the self-similar period is a key point in the study of mixing layers: this choice remains complex and the diversity of the criteria used for the selection process contributes to the diversity of results reported in the literature (also translating into the diversity of  $\delta_\theta = f(M_c)$  plots). Care has been given in the present study to a well-justified selection of this self-similar period, based on the analysis of the integrated streamwise production over time, which is proportional to the momentum thickness growth rate under certain conditions (Vreman *et al.* 1996).

Looking at the evolution of the integrated transport term over time enables the identification of the exit of turbulent structures from the computational domain, which is an appropriate criterion to define the end of the self-similar period. The sensitivity of the results to mesh refinement has also been investigated. The comparison of the present results obtained for air with the previous DNS of Pantano & Sarkar (2002) shows a good agreement and validates the present DNS of a compressible mixing layer in air described with the PG EoS.

The comparison between PG and DG does not show major differences for the momentum thickness growth rates and between the two TKE budgets. The DG seems to face the same well-known compressibility-related reduction of the momentum thickness growth rate, caused by the reduction of both pressure fluctuations and the gradient of the velocity fluctuations leading to the reduction of the pressure–strain terms. However, when these quantities are analysed at each turbulent scale, distributions over the wavenumbers turn out to be quite different between PG and DG. Results suggest that the DG effect yields an increase of the TKE at small scales.

Because of a significant decrease in the speed of sound, very large turbulent Mach numbers are expected to be observed experimentally when using DGs for thermodynamic states located in the inversion region. The turbulent Mach number is limited in the present study to approximately 0.4 on the centreline during the self-similar period and only briefly increases beyond 0.5 during the unstable growth

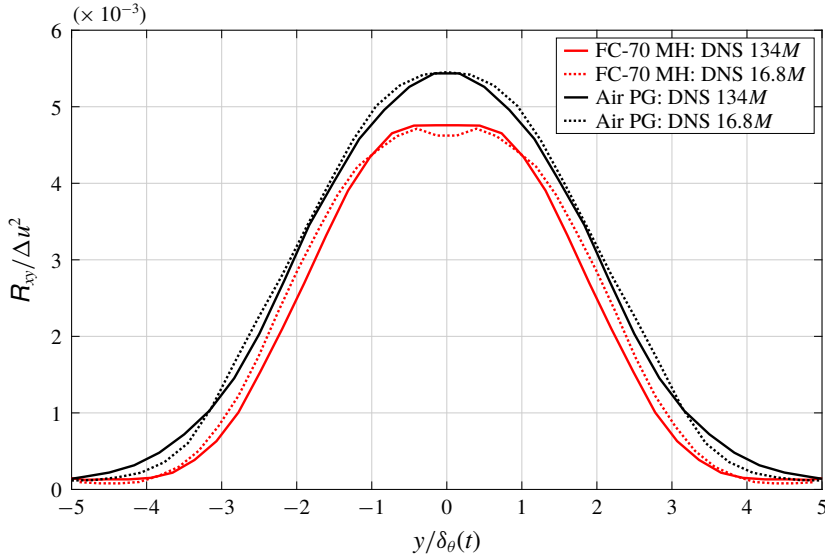


FIGURE 21. Distribution of the  $xy$  component of the turbulent stress tensor ( $R_{xy} = \overline{\rho u_x'' u_y''} / \bar{\rho}$ ) averaged over the self-similar period. Comparison is made between the 16.8M and the 134M simulations for DG and PG. Distributions have been averaged between the upper and the lower stream to get perfectly symmetric distributions.

phase. The analysis of a DG shear layer at a convective Mach number well above 1.1 will allow one to assess and possibly expand the conclusions drawn from the present comparison between DG and PG to highly supersonic or hypersonic flows.

### Acknowledgements

This work is supported by the JCJC ANR EDGES project, grant no. ANR-17-CE06-0014-01 of the French Agence Nationale de la Recherche. Simulations have been carried out using HPC resources at CINES under project grant no. A0042A07564.

### Declaration of interests

The authors report no conflict of interest.

### Appendix A. Domain size and resolution

Additional proofs of grid convergence are given in figures 20 and 21. Spectra and the  $xy$  component of the turbulent stress tensor computed for the 134M and the 16.8M simulations during the self-similar period are found to be very close, demonstrating a proper grid convergence of the results. For spectra, discrepancies occur at very small scales only, where energy is very low. This shows that the energy decrease for the 16.8M simulations starts at  $k_x/k_0 \approx 150$ , corresponding to about 1/2 to 1/3 of the Nyquist–Shannon sampling frequency. This observation appears very reasonable, given the third-order spatial accuracy of the numerical scheme.

To complement the grid resolution study, figure 22 displays a comparison between DG and PG for the vertical distribution of  $r = L_\eta / \Delta x$  at different non-dimensional times within the self-similar range. At the centre of the mixing layer, the Kolmogorov

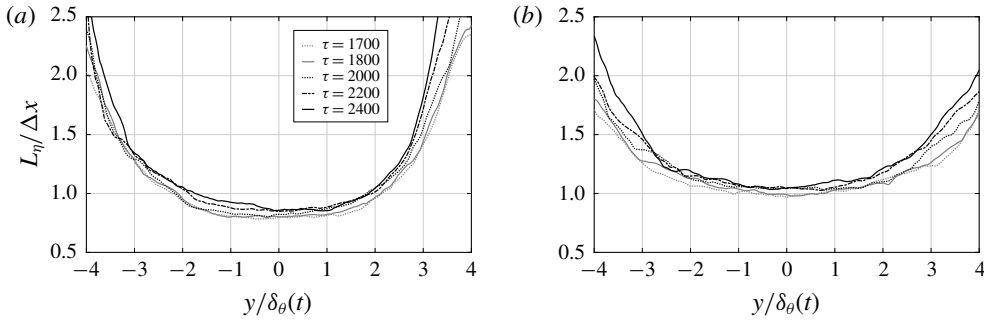


FIGURE 22. Distributions of  $r = L_\eta / \Delta x$ , the ratio between the Kolmogorov scale and the grid cell size, for the DG (a) and the PG (b) at several non-dimensional times inside the self-similar period ( $\tau \in \{1700; 1800; 2000; 2200; 2400\}$ ). Results are computed from the 134M simulation.

	$M_c$	$Re_{\delta_\theta}$	$Re_{\lambda_x}$	$r = L_\eta / \Delta x$	$l_x / L_x$	$l_z / L_z$
Air ( $\tau = 1700$ )	1.1	1874	143	0.97	0.073	0.063
Air ( $\tau = 2550$ )	1.1	2413	156	1.09	0.124	0.076
FC-70 ( $\tau = 1700$ )	1.1	2469	176	0.80	0.089	0.052
FC-70 ( $\tau = 2550$ )	1.1	3304	241	0.87	0.197	0.053

TABLE 3. Non-dimensional parameters computed at the beginning ( $\tau = 1700$ ) and at the end ( $\tau = 2550$ ) of the self-similar period. Parameter  $Re_{\lambda_x}$  denotes the Reynolds number based on the longitudinal Taylor microscale  $\lambda_x$  (see (4.2)) computed at the centreline and  $L_\eta$  denotes the Kolmogorov length scale computed at the centreline.

length scale is at its minimum value since the turbulent activity is maximum. A slightly better resolution at the centre can be observed for PG compared to DG, but values of  $r$  stay above 0.80 in any case, which is enough for DNS resolution. As a comparison, the ratio of Pantano & Sarkar (2002) was about 0.38.

Profiles are also different between PG and DG. The DG mixing layer is much more localized at the centre of the domain unlike the PG mixing layer which produces a wider distribution as noted in § 4.3.

Table 3 provides non-dimensional physical parameters of the simulation at the beginning ( $\tau = 1700$ ) and at the end ( $\tau = 2550$ ) of the self-similar period. Reynolds numbers based on the momentum thickness increase during the self-similar period and are large enough to lead to a turbulent flow, which is slightly more turbulent for the DG when compared to the PG. Reynolds numbers based on the longitudinal Taylor microscale are larger for DG compared to PG consistent with figure 16. The ratio  $r$  between the Kolmogorov scale and the grid cell size ( $L_\eta / \Delta x$ ) indicates the proper resolution of the simulation. The integral lengths  $l_x$  and  $l_z$  are computed using the streamwise velocity field:

$$l_x = \frac{1}{2\overline{u_x^2}} \int_{-L_x/2}^{L_x/2} \overline{u_x(\mathbf{x})u_x(\mathbf{x} + r\mathbf{e}_x)} dr, \tag{A 1}$$

$$l_z = \frac{1}{2\overline{u_x^2}} \int_{-L_z/2}^{L_z/2} \overline{u_x(\mathbf{x})u_x(\mathbf{x} + r\mathbf{e}_z)} dr, \tag{A 2}$$

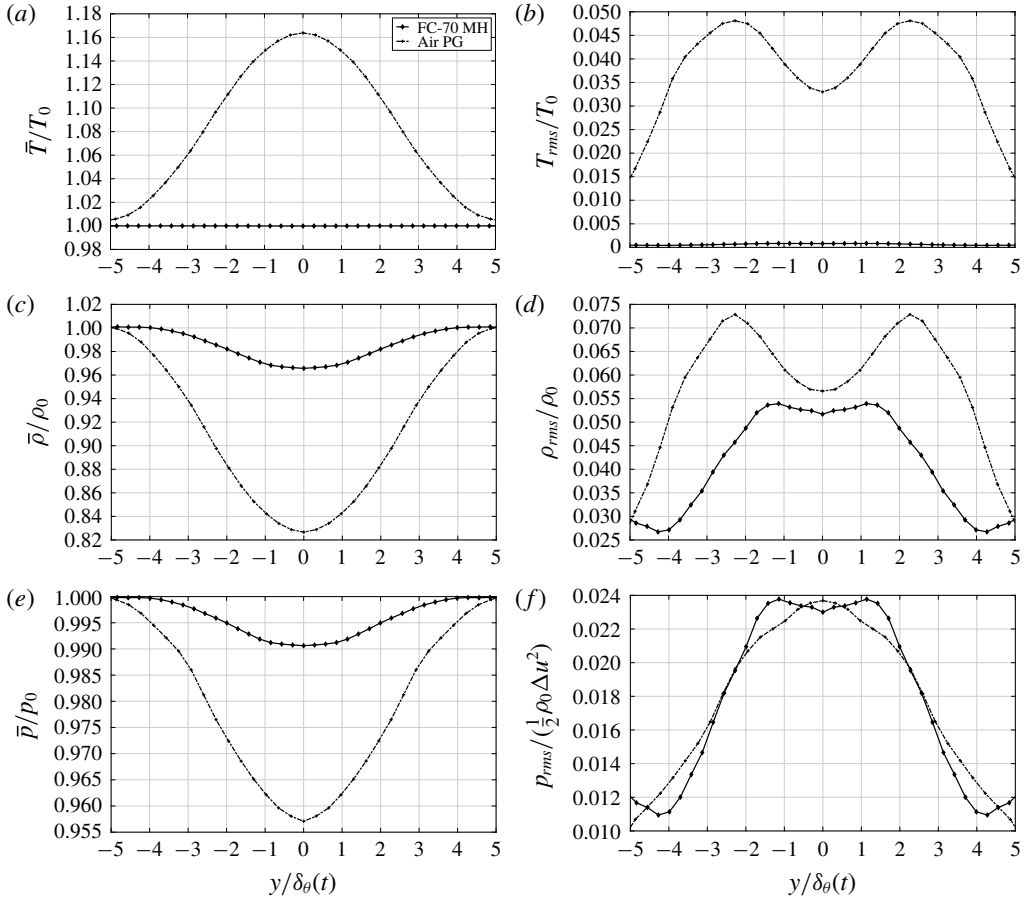


FIGURE 23. The non-dimensional Reynolds-averaged (*a,c,e*) and root-mean-square (*b,d,f*) values of temperature (*a,b*), density (*c,d*) and pressure (*e,f*) are averaged over the self-similar period ( $\tau \in [1700; 2550]$ ), plotted along the  $y$  direction and compared between FC-70 using the MH EoS and air using the PG EoS. Results are computed from the 134M simulation.

where  $\mathbf{e}_x$  and  $\mathbf{e}_z$  correspond to the unit vectors in the  $x$  and  $z$  directions, respectively. The computed integral lengths in the present study are larger than those in the simulation reported by Pantano & Sarkar (2002), with an integral length in the streamwise direction of about 0.03 for the same  $M_c = 1.1$  configuration but reaching 0.178 for a configuration with  $M_c = 0.7$  and a density ratio of 4. Despite these larger values for  $l_x$ , the computational domain appears to be still sufficiently large to ensure it does not disturb the development of turbulent structures. The same conclusion applies to the spanwise integral length scales for DG and PG.

**Appendix B. Mean and fluctuating thermodynamic quantities in the self-similar stage**

Figure 23 provides a comparison of pressure, temperature and density between DG and PG flows over the self-similar period. For PG, when looking at the Reynolds-averaged values, one can notice an increase of about 16 % of the temperature



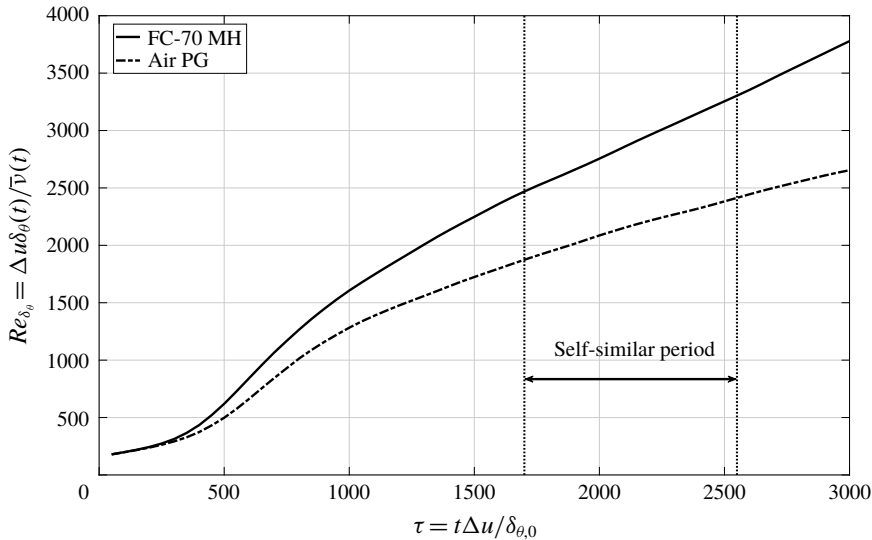


FIGURE 24. Temporal evolution of Reynolds number based on the momentum thickness. Results are computed from the 134M simulation.

at the centre of the mixing layer, due to viscous dissipation. Density decreases in similar proportions unlike pressure which is less impacted (4.5% decrease). For DG, the temperature is almost not affected by the viscous dissipation. Due to the molecular complexity of DG flows, the thermodynamic evolution is almost isothermal as already observed by Sciacovelli *et al.* (2017b).

When looking at the root-mean-square values of the fluctuations for PG, significant temperature fluctuations occur at the edges of the mixing layer due to turbulent mixing, leading to significant density variations. Pressure fluctuations are maximum at the centre of the mixing layer. For DG, temperature fluctuations are suppressed. Pressure fluctuations in the DG mixing layer are very close to fluctuations observed in the PG mixing layer, which is consistent with the same pressure–strain levels found in figures 14 and 15.

### Appendix C. Additional comparison during the self-similar period

Figure 24 provides a comparison between FC-70 and air for the Reynolds numbers based on the momentum thickness ( $Re_{\delta_0}$ ). These Reynolds numbers are computed using the domain-averaged viscosity. Results show a much larger increase of the Reynolds number during the whole evolution for DG compared to PG. During the unstable growth phase, this seems consistent with §4.2. However, during the self-similar period, the gap between DG and PG becomes larger and tends to increase. This behaviour is explained by an increase of the viscosity for PG due to the increase of the temperature (see figure 23). Since the flows are significantly turbulent, this difference in the Reynolds number evolution between DG and PG does not influence the mixing layer growth rates.

Figure 25 gives the profiles of  $xx$ ,  $yy$ ,  $zz$  and  $xy$  components of root-mean-square velocities for PG and DG. The self-similar period selected ( $\tau \in [1700; 2550]$ ) seems well confirmed by these distributions which collapse relatively well in this time interval. At  $\tau = 1000$ , the profiles are clearly not self-similar. At  $\tau = 1400$ , it is

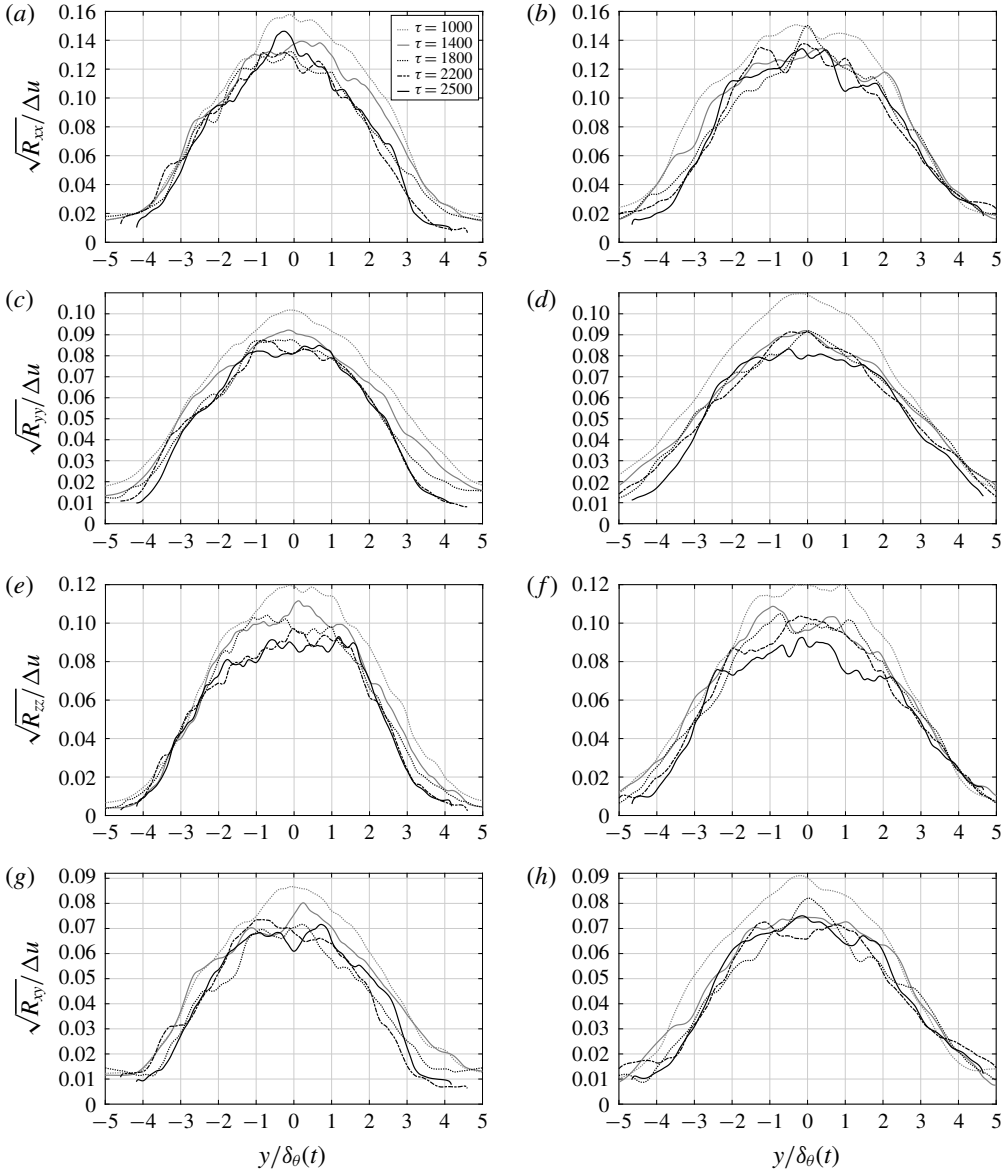


FIGURE 25. Distributions of the non-dimensional root-mean-square velocities ( $xx$  (a,b),  $yy$  (c,d),  $zz$  (e,f) and  $xy$  (g,h) components) for the DG (a,c,e,g) and the PG (b,d,f,h) at several non-dimensional times outside ( $\tau \in \{1000; 1400\}$ ) and inside ( $\tau \in \{1800; 2200; 2500\}$ ) the self-similar period. Results are computed from the 134M simulation.

less obvious to decide whether self-similarity is already achieved or not. In order to define the self-similar period from the root-mean-square velocity distributions, one can follow the method given in Almagro, García-Villalba & Flores (2017) computing the temporal mean and standard deviation of the Reynolds stresses for several time intervals. In this paper, another methodology is retained to define the self-similar period (see § 3.1). The comparison between DG and PG in figure 25 shows a similar

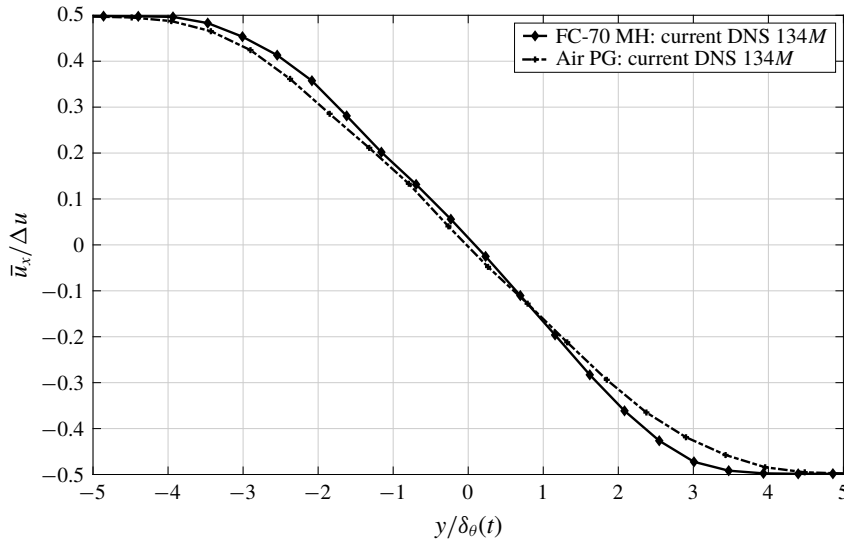


FIGURE 26. Distribution of the non-dimensional mean streamwise velocity averaged over the self-similar period. Comparison is made between FC-70 using the MH EoS and air using the PG EoS. Results are computed from the 134M simulation.

evolution for the four computed components. The peak value averaged over the self-similar period is about 0.14 and 0.09, respectively, for the  $xx$  and  $yy$  components, which is in good agreement with (Pantano & Sarkar 2002) where these values are reported as 0.14 and 0.10.

Figure 26 displays the distribution of the mean streamwise velocity for the DG and the PG shear layers. These profiles confirm the effect highlighted in §4.3, namely a slower propagation at the boundaries of the domain for DG compared with PG.

#### REFERENCES

- ALMAGRO, A., GARCÍA-VILLALBA, M. & FLORES, O. 2017 A numerical study of a variable-density low-speed turbulent mixing layer. *J. Fluid Mech.* **830**, 569–601.
- ALUIE, H. 2013 Scale decomposition in compressible turbulence. *Physica D* **247** (1), 54–65.
- ANDERS, J. B., ANDERSON, W. K. & MURTHY, A. V. 1999 Transonic similarity theory applied to a supercritical airfoil in heavy gas. *J. Aircraft* **36** (6), 957–964.
- ARGROW, B. M. 1996 Computational analysis of dense gas shock tube flow. *Shock Waves* **6** (4), 241–248.
- BAILLY, C. & COMTE-BELLOT, G. 2003 Turbulence. *Sciences et techniques de l'ingénieur*, CNRS Editions.
- BARRE, S. & BONNET, J. P. 2015 Detailed experimental study of a highly compressible supersonic turbulent plane mixing layer and comparison with most recent DNS results: towards an accurate description of compressibility effects in supersonic free shear flows. *Intl J. Heat Fluid Flow* **51**, 324–334.
- BATCHELOR, G. K. 1953 *The Theory of Homogeneous Turbulence*. Cambridge University Press.
- BETHE, H. A. 1942 The theory of shock waves for an arbitrary equation of state. *Res. and Dev. Tech. Paper* 545.
- BOGDANOFF, D. W. 1983 Compressibility effects in turbulent shear layers. *AIAA J.* **21** (6), 926–927.

- BORISOV, A. A., BORISOV, A. A., KUTATELADZE, S. S. & NAKORYAKOV, V. E. 1983 Rarefaction shock wave near the critical liquid–vapour point. *J. Fluid Mech.* **126**, 59–73.
- BRADSHAW, P. 1966 The effect of initial conditions on the development of a free shear layer. *J. Fluid Mech.* **26** (2), 225–236.
- BRADSHAW, P. 1977 Compressible turbulent shear layers. *Annu. Rev. Fluid Mech.* **9** (1), 33–52.
- BREIDENTHAL, R. E. 1992 Sonic eddy—a model for compressible turbulence. *AIAA J.* **30** (1), 101–104.
- BROWN, B. P. & ARGROW, B. M. 1998 Nonclassical dense gas flows for simple geometries. *AIAA J.* **36** (10), 1842–1847.
- BROWN, G. L. & ROSHKO, A. 1974 On density effects and large structure in turbulent mixing layers. *J. Fluid Mech.* **64** (4), 775–816.
- DE BRUIN, I. 2001 Direct and large-eddy simulation of the spatial turbulent mixing layer. PhD thesis, Eindhoven University of Technology.
- CADIEUX, F., DOMARADZKI, J. A., SAYADI, T., BOSE, T. & DUCHAINE, F. 2012 DNS and LES of separated flows at moderate Reynolds numbers. In *Proceedings of the 2012 Summer Program*, pp. 77–86. Center for Turbulence Research, NASA Ames/Stanford University.
- CHUNG, T. H., AJLAN, M., LEE, L. L. & STARLING, K. E. 1988 Generalized multiparameter correlation for nonpolar and polar fluid transport properties. *Ind. Engng Chem. Res.* **27** (4), 671–679.
- CINNELLA, P. & CONGEDO, P. M. 2005 Aerodynamic performance of transonic Bethe–Zel’dovich–Thompson flows past an airfoil. *AIAA J.* **43** (2), 370–378.
- CINNELLA, P. & CONGEDO, P. M. 2007 Inviscid and viscous aerodynamics of dense gases. *J. Fluid Mech.* **580**, 179–217.
- COLIN, O. & RUDGYARD, M. 2000 Development of high-order Taylor–Galerkin schemes for LES. *J. Comput. Phys.* **162** (2), 338–371.
- COLONNA, P. & GUARDONE, A. 2006 Molecular interpretation of nonclassical gas dynamics of dense vapors under the van der Waals model. *Phys. Fluids* **18** (5), 056101.
- COLONNA, P., GUARDONE, A., NANNAN, N. R. & ZAMFIRESCU, C. 2008 Design of the dense gas flexible asymmetric shock tube. *Trans. ASME J. Fluids Engng* **130** (3), 034501.
- COLONNA, P. & REBAY, S. 2004 Numerical simulation of dense gas flows on unstructured grids with an implicit high resolution upwind Euler solver. *Intl J. Numer. Meth. Fluids* **46** (7), 735–765.
- CONGEDO, P. M., CORRE, C. & CINNELLA, P. 2007 Airfoil shape optimization for transonic flows Bethe–Zel’dovich–Thompson fluids. *AIAA J.* **45** (6), 1303–1316.
- CONGEDO, P. M., CORRE, C. & CINNELLA, P. 2011 Numerical investigation of dense-gas effects in turbomachinery. *Comput. Fluids* **49** (1), 290–301.
- COSTELLO, M. G., FLYNN, R. M. & OWENS, J. G. 2000 Fluoroethers and fluoroamines. In *Kirk–Othmer Encyclopedia of Chemical Technology*. John Wiley & Sons.
- CRAMER, M. S. 1989 Negative nonlinearity in selected fluorocarbons. *Phys. Fluids A* **1** (11), 1894–1897.
- CRAMER, M. S. 1991 Nonclassical dynamics of classical gases. In *Nonlinear Waves in Real Fluids*, pp. 91–145. Springer.
- CRAMER, M. S. & CRICKENBERGER, A. B. 1991 The dissipative structure of shock waves in dense gases. *J. Fluid Mech.* **223**, 325–355.
- CRAMER, M. S. & KLUWICK, A. 1984 On the propagation of waves exhibiting both positive and negative nonlinearity. *J. Fluid Mech.* **142**, 9–37.
- CRAMER, M. S. & PARK, S. 1999 On the suppression of shock-induced separation in Bethe–Zel’dovich–Thompson fluids. *J. Fluid Mech.* **393**, 1–21.
- CRAMER, M. S. & SEN, R. 1986 Shock formation in fluids having embedded regions of negative nonlinearity. *Phys. Fluids* **29** (7), 2181–2191.
- DAI, Q., JIN, T., LUO, K. & FAN, J. 2018 Direct numerical simulation of particle dispersion in a three-dimensional spatially developing compressible mixing layer. *Phys. Fluids* **30** (11), 113301.
- DESOUTTER, G., HABCHI, C., CUENOT, B. & POINSOT, T. 2009 DNS and modeling of the turbulent boundary layer over an evaporating liquid film. *Intl J. Heat Mass Transfer* **52** (25–26), 6028–6041.

- DURA GALIANA, F. J., WHEELER, A. P. S. & ONG, J. 2016 A study of trailing-edge losses in organic rankine cycle turbines. *J. Turbomach.* **138** (12), 121003.
- FERGASON, S. H. & ARGROW, B. M. 2001 Simulations of nonclassical dense gas dynamics. In *35th AIAA Thermophysics Conference, Anaheim, CO*.
- FERGASON, S. H., HO, T. L., ARGROW, B. M. & EMANUEL, G. 2001 Theory for producing a single-phase rarefaction shock wave in a shock tube. *J. Fluid Mech.* **445**, 37–54.
- FREUND, J. B., LELE, S. K. & MOIN, P. 2000 Compressibility effects in a turbulent annular mixing layer. Part 1. Turbulence and growth rate. *J. Fluid Mech.* **421**, 229–267.
- FROM, C. S., SAURET, E., ARMPFIELD, S. W., SAHA, S. C. & GU, Y. T. 2017 Turbulent dense gas flow characteristics in swirling conical diffuser. *Comput. Fluids* **149**, 100–118.
- FU, S. & LI, Q. 2006 Numerical simulation of compressible mixing layers. *Intl J. Heat Fluid Flow* **27** (5), 895–901.
- GARNIER, E., ADAMS, N. & SAGAUT, P. 2009 *Large Eddy Simulation for Compressible Flows*. Springer Science & Business Media.
- GIAUQUE, A., CORRE, C. & MENGHETTI, M. 2017 Direct numerical simulations of homogeneous isotropic turbulence in a dense gas. *J. Phys.: Conf. Ser.* **821** (1), 012017.
- GRIESER, D. R. & GOLDTHWAITE, W. H. 1963 Experimental determination of the viscosity of air in the gaseous state at low temperatures and pressures. *Tech. Rep.* Battelle Memorial Institute, Columbus, OH.
- GUARDONE, A., VIGEVANO, L. & ARGROW, B. M. 2004 Assessment of thermodynamic models for dense gas dynamics. *Phys. Fluids* **16** (11), 3878–3887.
- HARINCK, J., COLONNA, P., GUARDONE, A. & REBAY, S. 2010a Influence of thermodynamic models in two-dimensional flow simulations of turboexpanders. *J. Turbomach.* **132** (1), 011001.
- HARINCK, J., TURUNEN-SAARESTI, T., COLONNA, P., REBAY, S. & VAN BUIJTENEN, J. 2010b Computational study of a high-expansion ratio radial organic Rankine cycle turbine stator. *Trans. ASME J. Engng Gas Turbines Power* **132** (5), 054501.
- HAYES, W. D. 1958 The basic theory of gasdynamic discontinuities, fundamentals of gas dynamics. In *High Speed Aerodynamics and Jet Propulsion* (ed. H. W. Emmons), pp. 416–481. Princeton University Press.
- INVERNIZZI, C. M. 2010 Stirling engines using working fluids with strong real gas effects. *Appl. Therm. Engng* **30** (13), 1703–1710.
- KIRILOV, N. G. 2004 Analysis of modern natural gas liquefaction technologies. *Chem. Petrol. Engng* **40** (7–8), 401–406.
- KLUWICK, A. 2004 Internal flows of dense gases. *Acta Mech.* **169** (1–4), 123–143.
- KOLMOGOROV, A. N. 1941 The local structure of turbulence in incompressible viscous fluid for very large Reynolds numbers. *Dokl. Akad. Nauk SSSR* **30** (4), 299–303.
- KRITSUK, A. G., NORMAN, M. L., PAOLO PADOAN, A. N. D. & WAGNER, R. 2007 The statistics of supersonic isothermal turbulence. *Astrophys. J.* **665** (1), 416–431.
- KUTATELADZE, S. S., NAKORYAKOV, V. E. & BORISOV, A. A. 1987 Rarefaction waves in liquid and gas–liquid media. *Annu. Rev. Fluid Mech.* **19** (1), 577–600.
- LIEPMANN, H. W. & LAUFER, J. 1947 Investigations of free turbulent mixing. *NACA Tech. Note* 1257.
- LUO, K. H. & SANDHAM, N. D. 1994 On the formation of small scales in a compressible mixing layer. In *Direct and Large-Eddy Simulation I*, pp. 335–346. Springer.
- MARTIN, J. J. & HOU, Y. 1955 Development of an equation of state for gases. *AIChE J.* **2** (4), 142–151.
- MARTIN, J. J., KAPOOR, R. M. & DE NEVERS, N. 1959 An improved equation of state for gases. *AIChE J.* **5** (2), 159–160.
- MARTÍNEZ FERRER, P. J., LEHNASCH, G. & MURA, A. 2017 Compressibility and heat release effects in high-speed reactive mixing layers I. Growth rates and turbulence characteristics. *Combust. Flame* **180** (M), 284–303.
- MATHIJSSSEN, T., GALLO, M., CASATI, E., NANNAN, N. R., ZAMFIRESCU, C., GUARDONE, A. & COLONNA, P. 2015 The flexible asymmetric shock tube (FAST): a Ludwig tube facility for

- wave propagation measurements in high-temperature vapours of organic fluids. *Exp. Fluids* **56** (10), 1–12.
- MENIKOFF, R. & PLOHR, B. J. 1989 The Riemann problem for fluid flow of real materials. *Rev. Mod. Phys.* **61** (1), 75.
- MERLE, X. & CINNELLA, P. 2014 Bayesian quantification of thermodynamic uncertainties in dense gas flows. *Reliability Engng Syst. Safety* **134**, 305–323.
- MOIN, P. & MAHESH, K. 1998 Direct numerical simulation: a tool in turbulence research. *Annu. Rev. Fluid Mech.* **30** (1), 539–578.
- MONACO, J. F., CRAMER, M. S. & WATSON, L. T. 1997 Supersonic flows of dense gases in cascade configurations. *J. Fluid Mech.* **330**, 31–59.
- OKONG’O, N. A. & BELLAN, J. 2002 Direct numerical simulation of a transitional supercritical binary mixing layer: heptane and nitrogen. *J. Fluid Mech.* **464**, 1–34.
- PANTANO, C. & SARKAR, S. 2002 A study of compressibility effects in the high-speed turbulent shear layer using direct simulation. *J. Fluid Mech.* **451**, 329–371.
- PAPAMOSCHOU, D. & ROSHKO, A. 1988 The compressible turbulent shear layer: an experimental study. *J. Fluid Mech.* **197**, 453–477.
- PIROZZOLI, S., BERNARDINI, M., MARIÉ, S. & GRASSO, F. 2015 Early evolution of the compressible mixing layer issued from two turbulent streams. *J. Fluid Mech.* **777**, 196–218.
- POINSOT, T. J. & LELE, S. K. 1992 Boundary conditions for direct simulations of compressible viscous flows. *J. Comput. Phys.* **101** (1), 104–129.
- ROGERS, M. M. & MOSER, R. D. 1994 Direct simulation of a self-similar turbulent mixing layer. *Phys. Fluids* **6** (2), 903–923.
- RUSAK, Z. & WANG, C.-W. 1997 Transonic flow of dense gases around an airfoil with a parabolic nose. *J. Fluid Mech.* **346**, 1–21.
- SANDHAM, N. D. & REYNOLDS, W. C. 1990 Compressible mixing layer – linear theory and direct simulation. *AIAA J.* **28** (4), 618–624.
- SARKAR, S. 1995 The stabilizing effect of compressibility in turbulent shear flow. *J. Fluid Mech.* **282**, 163–186.
- SARKAR, S., ERLEBACHER, G., HUSSAINI, M. Y. & KREISS, H. O. 1991 The analysis and modelling of dilatational terms in compressible turbulence. *J. Fluid Mech.* **227**, 473–493.
- SARKAR, S. & LAKSHMANAN, B. 1991 Application of a Reynolds stress turbulence model to the compressible shear layer. *AIAA J.* **29** (5), 743–749.
- SCIACOVELLI, L., CINNELLA, P., CONTENT, C. & GRASSO, F. 2016 Dense gas effects in inviscid homogeneous isotropic turbulence. *J. Fluid Mech.* **800**, 140–179.
- SCIACOVELLI, L., CINNELLA, P. & GLOERFELT, X. 2017a Direct numerical simulations of supersonic turbulent channel flows of dense gases. *J. Fluid Mech.* **821**, 153–199.
- SCIACOVELLI, L., CINNELLA, P. & GRASSO, F. 2017b Small-scale dynamics of dense gas compressible homogeneous isotropic turbulence. *J. Fluid Mech.* **825**, 515–549.
- SHUELY, W. J. 1996 Model liquid selection based on extreme values of liquid state properties in a factor analysis. *Tech. Rep.* Edgewood Research Development and Engineering Center, Aderbeen Proving Ground, MD.
- SPINELLI, A., DOSSENA, V., GAETANI, P., OSNAGHI, C. & COLOMBO, D. 2010 Design of a test rig for organic vapours. In *ASME Turbo Expo 2010: Power for Land, Sea, and Air*, pp. 109–120. Paper N.
- SPINELLI, A., PINI, M., DOSSENA, V., GAETANI, P. & CASELLA, F. 2013 Design, simulation, and construction of a test rig for organic vapors. *Trans. ASME J. Engng Gas Turbines Power* **135** (4), 042304.
- STEPHAN, K. & LAESECKE, A. 1985 The thermal conductivity of fluid air. *J. Phys. Chem. Ref. Data* **14** (1), 227–234.
- STULL, D. R. & PROPHET, H. 1971 Janaf thermochemical tables. *Tech. Rep.* National Standard Reference Data System.
- SUTHERLAND, W. 1893 LII. The viscosity of gases and molecular force. *Lond. Edin. Dublin Phil. Mag. J. Sci.* **36** (223), 507–531.

- TANAHASHI, M., IWASE, S. & MIYAUCHI, T. 2001 Appearance and alignment with strain rate of coherent fine scale eddies in turbulent mixing layer. *J. Turbul.* **2** (6), 1–17.
- THOMPSON, P. A. 1971 A fundamental derivative in gasdynamics. *Phys. Fluids* **14** (9), 1843–1849.
- THOMPSON, P. A. & LAMBRAKIS, K. C. 1973 Negative shock waves. *J. Fluid Mech.* **60** (1), 187–208.
- VADROT, A., GIAUQUE, A. & CORRE, C. 2019 Investigation of turbulent dense gas flows with direct numerical simulation. In *Congrès français de mécanique*. AFM.
- VREMAN, A. W., SANDHAM, N. D. & LUO, K. H. 1996 Compressible mixing layer growth rate and turbulence characteristics. *J. Fluid Mech.* **320**, 235–258.
- WAGNER, B. & SCHMIDT, W. 1978 Theoretical investigations of real gas effects in cryogenic wind tunnels. *AIAA J.* **16** (6), 580–586.
- WANG, C.-W. & RUSAK, Z. 1999 Numerical studies of transonic BZT gas flows around thin airfoils. *J. Fluid Mech.* **396**, 109–141.
- WANG, J., WAN, M., CHEN, S. & CHEN, S. 2018 Kinetic energy transfer in compressible isotropic turbulence. *J. Fluid Mech.* **841**, 581–613.
- WHEELER, A. P. S. & ONG, J. 2013 The role of dense gas dynamics on organic Rankine cycle turbine performance. *Trans. ASME J. Engng Gas Turbines Power* **135** (10), 102603.
- WHITE, F. M. 1998 *Fluid Mechanics*. McGraw-Hill Series in Mechanical Engineering.
- ZEL'DOVICH, J. 1946 On the possibility of rarefaction shock waves. *Zh. Eksp. Teor. Fiz.* **16** (4), 363–364.
- ZEMAN, O. 1990 Dilatation dissipation: the concept and application in modeling compressible mixing layers. *Phys. Fluids A* **2** (2), 178–188.
- ZHOU, Q., HE, F. & SHEN, M. Y. 2012 Direct numerical simulation of a spatially developing compressible plane mixing layer: flow structures and mean flow properties. *J. Fluid Mech.* **711**, 1–32.